Diplomarbeit

Oxygen stoichiometry of A-site deficient perovskites for solid oxide cells

ausgeführt zum Zwecke der Erlangung des akademischen Grades eines
Diplom-Ingenieurs (Dipl.-Ing. oder DI)

Ausgeführt am Institut für Chemische Technologien und Analytik
der Technischen Universität Wien

unter der Leitung von
Univ.Prof. Dipl.Phys. Dr.rer.nat. Jürgen FLEIG
und Mitwirkung von
Univ.Ass. Dipl.-Ing. Dr.rer.nat. Andreas Nenning

durch

Stanislaus Breitwieser

Mat.Nr.: 01615888

Wien, am 04. September 2023

Unterschrift

TU Wien

Master's Thesis

Oxygen stoichiometry of A-site deficient perovskites for solid oxide cells

Author:
Stanislaus Breitwieser

Supervisors:
Univ.Prof. Dipl.Phys. Dr.rer.nat.
Jürgen Fleig

Univ.Ass. Dipl.-Ing. Dr.rer.nat.
Andreas Nenning

A thesis submitted in fulfilment of the requirements for the degree of
Master of Science at the

Institute of Chemical Technologies and Analytics

04.09.2023 , Vienna

Stanislaus Breitwieser

Abstract

The surface chemistry and thus in turn the oxygen exchange kinetics of perovskite-type electrode materials for solid oxid fuel cells (SOFCs) and solid oxid electrolysis cells (SOECs) is strongly affected by segregation phenomena. Typically, B-site cations segregate in form of catalytically active metal nanoparticles in reducing conditions, while A-site cations tend to segregate in oxidizing conditions and lead to performance loss. One possible way to enhance the desired segregation of B-site cations while simultaneously decreasing the undesired segregation of A-site cations is to employ A-site deficient materials. For a detailed understanding of the underlying mechanisms, precise knowledge of the oxygen vacancy concentration is of importance. In this study, A-site deficient $La_{0.6}Sr_{0.4}FeO_{2.8-\delta}$ (LSF) and $SrTi_{0.6}Fe_{0.4}O_{2.8-\delta}$ (STF) serve as model materials. We present a new miniature coulometric titration cell that allows for precise measurements of changes in the oxygen non-stoichiometry of LSF and STF powder samples over a wide pO_2 range. Additionally, we applied the same principle to electrochemical cells with thin film STF electrodes, on which irreversible processes could be determined more precisely. The presented methods not only allow for the quantification of changes in oxygen stoichiometry, but also for the quantification of easily reducible secondary phases that either come from synthesis, or form in-situ during electrochemical reduction. Moreover, we can show how the bulk oxygen vacancy concentration is linked to transition metal oxidation states on the surface that were determined by in-situ X-ray photoelectron spectroscopy (XPS) measurements on electrochemically polarized model cells.

Kurzfassung

Die Oberflächenchemie und damit die Sauerstoffaustauschkinetik von Elektrodenmaterialien mit Perowskit Struktur für Festoxid-Brennstoffzellen (eng.: Solid oxide fuell cells (SOFC)) und Festoxid-Elektrolysezellen (eng.: solid oxid electrolysis cells (SOEC)) wird stark von Segregationsphänomenen beeinflusst. Typischerweise segregieren Kationen am B-Platz bei reduzierenden Bedingungen unter Bildung katalytisch aktiver Nanopartikel, wohingegen die Segregation von Kationen am A-Platz bei oxidierenden Bedingungen zu Leistungsverlusten führt. Eine Möglichkeit, die erwünschte Segregation von B-Platz Kationen zu fördern und gleichzeitig die unerwünschte Segregation von A-Platz Kationen zu verringern, ist die Verwendung von Materialien mit A-Platz defizit. Für ein detailliertes Verständnis der zugrundeliegenden Mechanismen ist eine genaue Kenntnis der Sauerstoffleerstellen-Konzentration von Bedeutung. In dieser Arbeit stellen wir eine neue coulometrische miniatur Titrierzelle vor, die präzise Messungen von Änderungen der Sauerstoff-Nichtstöchiometrie von Pulverproben über einen breiten pO_2-Bereich ermöglicht. A-Platz defizitäres $La_{0.6}Sr_{0.4}FeO_{2.8-\delta}$ (LSF) und $SrTi_{0.6}Fe_{0.4}O_{2.8-\delta}$ (STF) dienen dabei als Modellmaterialien. Darüber hinaus haben wir das gleiche Prinzip auf elektrochemische Zellen mit STF Dünnschicht-Elektroden angewandt, an denen irreversible Prozesse genauer bestimmt werden können. Die vorgestellten Methoden ermöglichen nicht nur die Quantifizierung von Änderungen der Sauerstoffstöchiometrie, sondern auch die Quantifizierung leicht reduzierbarer Sekundärphasen, die entweder aus der Synthese stammen oder sich in-situ während der elektrochemischen Reduktion bilden. Des Weiteren konnten wir zeigen, wie die Sauerstoff-Lehrstellenkonzentration mit den Oxidationszuständen der Übergangsmetalle an der Oberfläche zusammenhängt, die durch In-situ-Röntgenphotoelektronenspektroskopie (eng.: X-ray photoelectron spectroscopy (XPS)) an elektrochemisch polarisierten Modellzellen bestimmt wurden.

List of Symbols

The following list comprises variables and constant that will be used in this work

Physical constants

F	Faraday constant 96 485.332 $\frac{\mathrm{C}}{\mathrm{mol}}$
R	Ideal gas constant 8.314463 $\frac{\mathrm{J}}{\mathrm{mol \cdot K}}$

Variables

δ	Oxygen non-stoichiometry (per formula unit)
pO_2	Oxygen partial pressure (bar)
E	Voltage (V)
I	Current (A)
n	Amount of sample (mol)
Q	Charge (C)
R	Resistance (Ω)
T	Temperature (K)
t	Time (s)
vol%	Volume percent

w%	Weight percent
z	Number of transferred electrons

Contents

1 Introduction

As should nowadays not needed to be explained in further detail, energy storage and conversion are of undeniable importance to tackle enviromental and economic issues. Among the many devices employed in this field, Solid Oxide Fuel Cells (SOFCs) and Solid Oxide Electrolysis Cells (SOECs) offer unique advantages, such as high efficiencies and flexibility concerning utilised fuels [1]. Standard SOFCs consist of Yttria Stabilized Zirconia (YSZ) as electrolyte and cermets or perovskites as electrodes [1]. For perovskite-type electrodes, which are the focus of this work, activities strongly depend on the surface chemistry. Surface chemistry in turn can be dependent on segregation phenomena. As has been shown for different Sr containing perovskites, surface Sr segregation (in the presence of sulfur trace impurities in the feed gas) significantly increases the area specific resistance [2–4] *via* a mechanism proposed in [5]. Under reducing conditions, segregation of transition metals (such as Fe or Ni) has been observed to lead to the formation of nano-particles at the surface of a wide range of perovskite-type materials, which significantly increased catalytic activity [6–10].

In the above-described examples, segregation of the A-site ion leads to a degradation of the electrode, whereas segregation of the B-site ion leads to an improvement of the electrode. As a general way to promote the often desirable segregation of B-site ions while hindering the often unwanted segregation of A-site ions we propose the use of A-site deficient perovskites. This is based on the idea that the lower concentration of A-site ions in the bulk might lower the chemical potential of A-site ions in the bulk compared to the surface, thus minimising A-site segregation. On the other hand, the chemical potential of the B-site ion might be increased inside the bulk compared to the surface, supporting B-site segregation. This would allow to control the surface chemistry *via* the bulk composition. The effect of non-stoichiometry on the surface chemistry of some perovskites has been studied in [11–13], where A-site deficiency has promoted B-site segregation. A-site deficient perovskites have already shown improved electrochemical performance as oxygen electrodes [14, 15], for electrocatalytic N_2 reduction

[16] and for the oxygen reduction reaction at room temperature [17]. However, to study the effect of sub-stoichiometry on the defect chemistry of perovskite-type materials, new analysis methods are desired.

Herein, we present a new miniature coulometry cell to analyse powder samples. In addition, a method combining Electrochemical Impedance Spectroscopy (EIS) and coulometry to study thin film samples was employed. $La_{1-x}Sr_xFeO_{3-\delta}$ (LSF) and $SrTi_{1-x}Fe_xO_{3-\delta}$ (STF) powders of varying sub-stoichiometry were used as model systems to investigate the pO_2 dependency of the oxygen non-stoichiometry of A-site deficient materials. Powder samples were prepared *via* solid state synthesis as well as different modified Pechni synthesis routes. The phase purity of the different synthesis methods was compared. As phase pure powder samples with a high A-site deficiency can be difficult to obtain, STF thin film samples (prepared *via* Pulsed Laser Deposition (PLD) from A-site deficient targets) were analysed as well. X-Ray Photoelectron Spectroscopy (XPS) measurements were employed to validate the results from the coulometry. Inductively Coupled Plasma Mass Spectrometry (ICP-MS) measurements were performed to analyse the resulting sample stoichiometries. In addition to the analysis of the oxygen non-stoichiometry, the pO_2 dependency of oxygen exchange kinetics of the prepared thin films was studied *via* EIS.

2 Theoretical Background

2.1 Perovskite structure and defect chemistry

The perovskite crystal structure described by the general formula ABO_3 consists of a large A cation, which is cuboctahedrally coordinated by oxygen anions and a smaller B cation. The B cation is octahedrally coordinated by oxygen anions (a schematic of the structure is presented in fig. 2.1). Point defects in perovskites give rise to electrochemical functionality. The most important point defects are oxygen vacancies that lead to oxygen ion conductivity and mixed valence states (mostly of the B-site cation), which lead to electronic conductivity. Due to the possible occurrence of electronic as well as ionic defects in perovskites, many perovskites behave as Mixed Ion Electron Conductors (MIECs) in a certain pO_2 range. This makes them excellent candidates for the application in SOFCs and SOECs. Oxygen vacancies and electronic defects are coupled *via* eq. ((2.1)) (All defect reactions are denoted in Kröger-Vink notation, as described in [18]):

$$V_O^{\bullet\bullet} + \frac{1}{2} O_2 \rightleftharpoons 2\,h^{\bullet} + O_O^{\times}. \tag{2.1}$$

Electrons and electron holes are coupled by

$$\mathrm{nil} \rightleftharpoons h^{\bullet} + e^{-} \tag{2.2}$$

As the localization of electron holes can be complex [19], electron holes will be denoted in a general way. Electrons however, will be described as B_B' in the following, which is equivalent to e^- localized on the B-site. .

These defects are partly introduced by intrinsic oxygen incorporation/release equilibria eq. ((2.1)), but to a larger extent stem from extrinsic acceptor doping on the A-site and/or B-site. Furthermore, the A:B cation ratio may be slightly below 1, which leads to A-site vacancies and potentially anti-site defects. These defects are coupled due to charge neutrality given by

$$\sum_i \mathrm{z_i c_i} = 0. \tag{2.3}$$

Therein, $\mathrm{z_i}$ and $\mathrm{c_i}$ are the defect charge and concentration (per formula unit), respectively.

The intrinsic defect chemical reactions occur without doping, such as the formation of oxygen vacancies coupled with a valence state change of the B-site cation, expressed by the defect reaction

$$\mathrm{nil} \rightleftharpoons 2\,\mathrm{B}'_\mathrm{B} + \mathrm{V}_\mathrm{O}^{\bullet\bullet} + \frac{1}{2}\,\mathrm{O_2}. \tag{2.4}$$

Depending on the reducibility of the B-site cation and oxygen partial pressure, acceptor doping on the A-site may be coupled with the formation of oxygen vacancies:

$$2\,\mathrm{ABO_3} + 2\,\mathrm{XO} \xrightarrow{-\,\mathrm{A_2O_3}} 2\,\mathrm{X}'_\mathrm{A} + \mathrm{V}_\mathrm{O}^{\bullet\bullet}, \tag{2.5}$$

or with the formation of electron holes:

$$2\,\mathrm{ABO_3} + 2\,\mathrm{XO} + \frac{1}{2}\,\mathrm{O_2} \xrightarrow{-\,\mathrm{A_2O_3}} 2\,\mathrm{X}'_\mathrm{A} + 2\,\mathrm{h}^{\bullet} \tag{2.6}$$

Similarly, acceptor doping may also occur at the B-site, given by

$$2\,\mathrm{ABO_3} + \mathrm{X_2O_3} \xrightarrow{-\,2\,\mathrm{BO_2}} 2\,\mathrm{X}'_\mathrm{B} + \mathrm{V}_\mathrm{O}^{\bullet\bullet} + \frac{1}{2}\,\mathrm{O_2}. \tag{2.7}$$

In all these cases A and B ions are assumed in the ideal lattice $\mathrm{ABO_3}$.

For the purpose of this work, cation non-stochiometry, especially A-site deficiency is of importance as well. A-site deficiency can either be compensated *via* the formation of A-site vacancies or anti-site defects, as shown for A^{2+} and B^{4+} in ABO_3 by

$$\text{nil} \xrightarrow{-\ \text{AO}} V_A'' + V_O^{\bullet\bullet} \tag{2.8}$$

and

$$\text{nil} + V_O^{\bullet\bullet} \xrightarrow{-\ 2\,\text{AO}} B_A^{\bullet\bullet} + [V_A'' + V_B'''' + 3\,V_O^{\bullet\bullet}]_{\text{nil}} \tag{2.9}$$

Charge neutrality is achieved by the formation of oxygen vacancies or the formation of electronic defects, which are coupled *via* the equilibrium eq. ((2.1)).

A-site deficiency can thus act as an effective acceptor dopant if compensated by the formation of A-site vacancies or as donor dopant if compensated by the formation of anti-site defects. A-site vacancies and anti-site defects are coupled *via* the equlibrium given by

$$3\,V_O^{\bullet\bullet} + 2\,V_A'' \rightleftharpoons B_A^{\bullet\bullet} + [V_A'' + V_B'''' + 3\,V_O^{\bullet\bullet}]_{\text{nil}}. \tag{2.10}$$

Equilibrium constants for the three important equilibria presented above (eqs. ((2.1)), ((2.2)) and ((2.10))) can be described by eqs. ((2.11)) to ((2.13)):

$$K_{\text{oxygen incorporation}} = \frac{[h^\bullet]^2}{[V_O^{\bullet\bullet}]\,[O_2]^{1/2}}, \tag{2.11}$$

$$K_{\text{electron-hole pair}} = [h^\bullet][e^-], \tag{2.12}$$

$$K_{\text{anti-site}} = \frac{[B_A^{\bullet\bullet}]}{[V_O^{\bullet\bullet}]^3\,[V_A'']^2}. \tag{2.13}$$

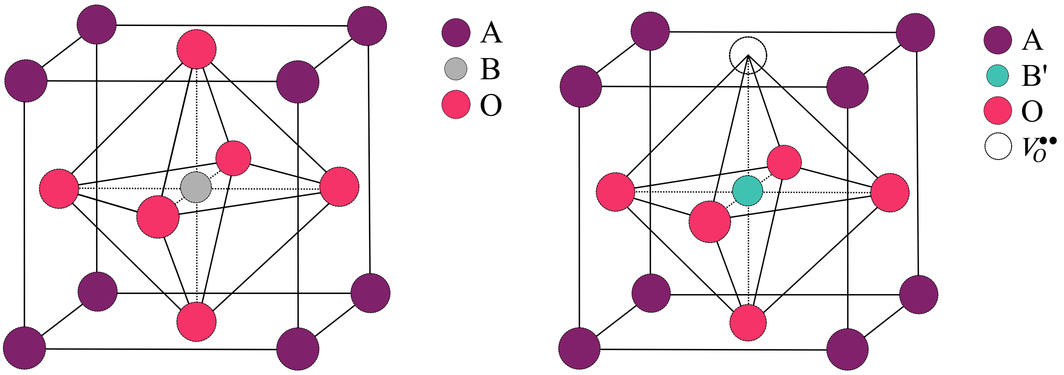

(a) Undoped perovskite **(b)** Doped perovskite with oxygen vacancy

FIGURE 2.1: Structure of doped and undoped perovskite

Please note, that site restriction is not considered in eqs. ((2.11)) to ((2.13)). These three equilibria are coupled to each other, so that A-site vacancies and anti-site defects can theoretically be compensated both by the formation of ionic and electronic defects.

2.2 Cation segregation in perovskites

The chemical environment at surfaces and interfaces of perovskite-type materials often clearly differs from the bulk material, which leads to different chemical potentials at the surface/interface compared to the bulk. This in turn can cause a preferential accumulation of one cation species at the surface/interface [20]. High temperatures and the wide pO_2 range present in SOFCs and SOECs promote these cation segregation phenomena, which can have a severe impact on the electrochemical performance of such electrodes. Segregation phenomena show a strong pO_2 dependence. Under reducing conditions, segregation of the B-site ions appears to be preferred, whereas oxidizing conditions tend to lead to the segregation of A-site ions [20]. Under working conditions, segregation of the A-site ion was found to decrease the oxygen exchange rate of the electrode material, whereas segregation of the B-site ion tends to increase catalytic activity, as shown for water splitting in [21] and [22]. A-site and B-site segregation can be described by

$$\mathrm{nil} + \frac{1}{2}\,\mathrm{O_2} \longrightarrow \mathrm{V_A''} + \mathrm{AO} + 2\,\mathrm{h^{\bullet}} \qquad (2.14)$$

as a sum of eq. ((2.1)) and eq. ((2.8)) for A-site ions and

$$3\,\mathrm{B}_\mathrm{B}^{\prime} \longrightarrow 2\,\mathrm{B}_\mathrm{B}^{\times} + \mathrm{B}^0 + \mathrm{V}_\mathrm{B}^{\prime\prime\prime} \tag{2.15}$$

for B-site ions,

for a doubly charged A-site ion and a triply charged B-site ion in a doped perovskite such as LSF, respectively.

2.3 $La_{1-x}Sr_xFeO_{3-\delta}$

The perovskite-type oxide LSF encompasses a group of materials behaving as a solid solution between $SrFeO_3$ and $LaFeO_3$. When viewed as Sr doped $LaFeO_3$, Sr on a La-site leads to a charge defect, that can be compensated according to [23] by.

$$\mathrm{LaFeO_3} \xrightarrow{\mathrm{SrFeO_3}} \mathrm{Sr}_\mathrm{La}^{\prime} + \frac{1}{2}\,\mathrm{V}_\mathrm{O}^{\bullet\bullet}. \tag{2.16}$$

The resulting oxygen vacancies are in equilibrium with electronic defects and the gas phase as described in eq. ((2.1)) [23].

This in turn leads to the total stoichiometry of $La_{1-x}Sr_xFeO_{3-x/2-\delta}$. At intermediate pO_2 (around 10^{-20} to 10^{-5} bar), this stoichiometry is stable with $\delta = 0$ over a wide pO_2 range [23]. An increase of pO_2 from this stoichiometry plateau leads to the formation of electron holes coupled with the incorporation of oxygen into the lattice in accordance with eq. ((2.1)). A reduction of pO_2 on the other hand leads to the formation of oxygen vacancies coupled with the transition of Fe^{3+} to Fe^{2+} in accordance with:

$$2\,\mathrm{Fe}_\mathrm{Fe}^{\times} \rightleftharpoons 2\,\mathrm{Fe}_\mathrm{Fe}^{\prime} + \mathrm{V}_\mathrm{O}^{\bullet\bullet} + \frac{1}{2}\,\mathrm{O}_2. \tag{2.17}$$

In fig. 2.2 the effect of the pO_2 on the oxygen stoichiometry (measured by coulometry and thermogravimetry) of LSF is presented [23]. Here, the above described trend is displayed.

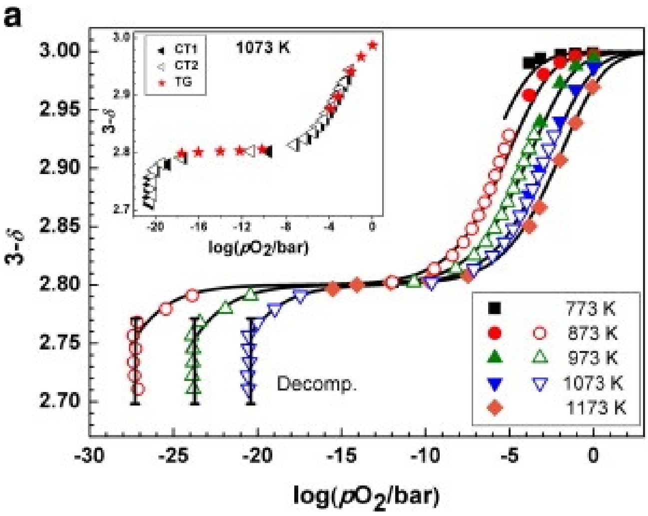

Figure 2.2: Oxygen stoichiometry vs pO_2 of $La_{0.6}Sr_{0.4}FeO_{3-\delta}$ at various temperatures. Data points were measured *via* coulometry and thermogravimetry. Here, in contrast to this work, the oxygen non-stoichiometry is related to the fully oxidised state ($La_{0.6}Sr_{0.4}FeO_3$) instead of the stoichiometry plateau ($La_{0.6}Sr_{0.4}FeO_{2.8}$). Reprinted with permission from [23]. Copyright 2011 Elsevier.

2.4 $SrTi_{1-x}Fe_xO_{3-\delta}$

The perovskite-type oxide STF encompasses a group of materials behaving as a solid solution between $SrTiO_3$ (STO) and $SrFeO_{2.5}$ (SFO) with $0 \leq x \leq 1$ [24]. An accurate description of the defect chemistry is the subject of scientific discourse [25]. For this work, however, a rather simple model shall suffice to explain the observed behaviour of STF. STF will be viewed as Fe doped STO (Fe:STO), with Fe randomly distributed on the Ti sub-lattice. At intermediate pO_2, when all Fe is trivalent, charge compensation of Fe^{3+} on a Ti site primarily takes place *via* the formation of oxygen vacancies according to eq. ((2.18)) [26]. This leads to a stoichiometry plateau with the effective composition $SrTi_{1-x}Fe_xO_{3-(x/2)}$ [25]. For the purpose of this work, this stoichiometry plateau will be viewed as a reference point to which changes in oxygen stoichiometry will be related.

$$\mathrm{SrTiO_3} \xrightarrow{\mathrm{Fe_2O_3}} 2\,\mathrm{Fe}'_{\mathrm{Ti}} + \mathrm{V}_{\mathrm{O}}^{\bullet\bullet} \tag{2.18}$$

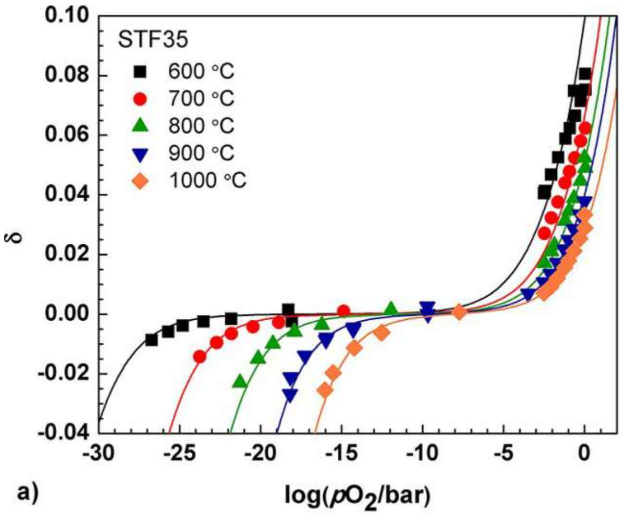

FIGURE 2.3: Oxygen stoichiometry vs pO_2 of $SrTi_{0.65}Fe_{0.35}O_{2.825-\delta}$ at various temperatures. Data points were measured *via* thermogravimetry. Reprinted with permission from [27]. Copyright 2013 American Chemical Society.

Increasing the pO_2 from the stoichiometry plateau leads to the incorporation of oxygen into the lattice, coupled with the formation of electron holes according to eq. ((2.1)) [26]. Reducing the oxygen partial pressure below the pO_2 of the stoichiometry plateau leads to the creation of new oxygen vacancies. Charge compensation can either be accomplished *via* the reduction of Fe^{3+} to Fe^{2+} (as described in eq. ((2.17))) or at very low oxygen partial pressures also *via* the reduction of Ti^{4+} to Ti^{3+}. The sum of these reactions leads to mixed ionic and electronic conductivity with a focus on *p*-type conductivity at high pO_2 ($> 10^{-1}$), ion conductivity at intermediate pO_2 (around 10^{-20} to 10^{-5} bar) and *n*-type conductivity at low pO_2 ($< 10^{-25}$ bar) [25]. A figure displaying the pO_2 dependency of the oxygen stoichiometry measured by thermogravimetry is presented in fig. 2.3 [27].

2.5 Coulometry

Coulometry is an electrochemical analytical method that is characterized by the quantification of the analyte *via* the quantification of the total charge necessary for the electrochemical conversion of the analyte. Measurements can be performed in potentiostatic (constant potential) or galvanostatic (constant current) mode. In potentiostatic mode, a fixed potential is applied to the sample and the resulting current (or charge) is monitored. In galvanostatic mode, the current is fixed and the resulting potential monitored. In both cases, the resulting data are charge-voltage pairs. The measured charge is then related to the amount of reacted analyte *via*

$$\text{Analyte}_{\text{reacted}} = \frac{Q}{\text{z} \cdot \text{F}}. \tag{2.19}$$

In the context of this work, the reacted analyte corresponds to the oxygen transfered to the sample.

For the measurement setups used, the voltage E (neglecting any overpotential) is related to the effective pO_2 *via*

$$\text{pO2}_{\text{inside}} = \text{pO2}_{\text{outside}} \cdot e^{\frac{4F}{RT} \cdot E}, \tag{2.20}$$

where $\text{pO2}_{\text{inside}}$ and $\text{pO2}_{\text{outside}}$ are the oxygen partial pressure inside and outside of the measuring cell, respectively.

Coulometry in this work was performed in a step wise motion. For potentiostatic measurements, each constant voltage step was held until the sample had equilibrated ($\frac{dI}{dt} = 0$), then the voltage was changed to a new setpoint. For galvanostatic measurements, each constant current step was followed by a rest step in order to let the sample equilibrate ($\frac{dE}{dt} = 0$).

3 Materials and Methods

3.1 List of chemicals

All chemicals used are listed in table 3.1.

Table 3.1: Overview of the used chemicals

Chemical Formula	Name	Purity	Supplier
H_2O	Bi-distilled water	-	-
EtOH	Ethanol	99.98	VWR Chemicals
HNO_3 (70 %)	Nitric acid (conc.)	99.999	Sigma Aldrich
$SrCO_3$	Strontium carbonate	99.9%	Sigma Aldrich
$Sr(NO_3)_2$	Strontium nitrate	99.99%	Merck
Fe_2O_3	Iron(III) oxide	99.99%	Alfa Aeser
$Fe(NO_3)_3 \cdot 9H_2O$	Iron(III) nitrate nonahydrate	99.99%	Sigma Aldrich
$Ti(OCH_2CH_2CH_2CH_3)_4$	Titatnium(IV) butoxide	97%	Sigma Aldrich
$HOC(COOH)(CH_2COOH)_2$	Citric acid	99.5%	Honeywell
TiO_2	Titanium(IV) oxide	99.995%	Alfa Aeser
$Y_{0.17}Zr_{0.83}O_{1.915}$	9.5 mol% YSZ single crystal	-	Mateck
$PrCeO_{2-\delta}$	PCO paste	-	-
Pt	Platinum paste	-	Tanaka
La_2O_3	Lanthanum oxide	99,999	Sigma Aldrich
$Gd_{0.1}Ce_{0.9}O_{2-\delta}$	GDC	-	Treibacher
O_2	Oxygen gas	99.999	Messer
N_2	Nitrogen gas	99.999	Messer
Ar/H_2 (2 %)	Hydrogen (2%) in argon	-	Messer
Fe (0.615 mol/l) in HNO_3 (70 %)	Fe-solution*	-	-
-	Ink vehicle	-	Fuelcellmaterials, USA
HCl (37 %)	Hydrochloric acid	p.a.	Merck
HF (40 %)	Hydroflouric acid	p.a.	Merck
Fe	Iron chips	99.98	Sigma Aldrich
$Y_{0.15}Zr_{0.85}O_{1.925}$	8 mol% YSZ powder	-	Tosoh

*prepared from metallic Fe and HNO_3

3.2 Synthesis and sample preparation

3.2.1 Powder samples

LSF and STF powder samples of varying A-site sub-stoichiometry were prepared *via* different synthesis routes to compare the suitability of the chosen synthesis routes to create phase pure samples. A list of all samples is presented in table 3.2.

Table 3.2: Overview of the prepared powder samples

Name	Stochiometry	Synthesis route
LSF6040	$La_{0.6}Sr_{0.4}FeO_{2.8-\delta}$	solid state
LSF57.540	$La_{0.575}Sr_{0.4}FeO_{2.8-\delta}$	solid state
LSF5040	$La_{0.5}Sr_{0.4}FeO_{2.8-\delta}$	solid state
STF100	$SrTi_{0.6}Fe_{0.4}O_{2.8-\delta}$	solid state
STF97	$Sr_{0.97}Ti_{0.6}Fe_{0.4}O_{2.8-\delta}$	solid state
STF95	$Sr_{0.95}Ti_{0.6}Fe_{0.4}O_{2.8-\delta}$	solid state
STF93	$Sr_{0.93}Ti_{0.6}Fe_{0.4}O_{2.8-\delta}$	solid state
STF97P	$Sr_{0.97}Ti_{0.6}Fe_{0.4}O_{2.8-\delta}$	modified Pechini
STF95P	$Sr_{0.95}Ti_{0.6}Fe_{0.4}O_{2.8-\delta}$	modified Pechini 2
STF93P	$Sr_{0.93}Ti_{0.6}Fe_{0.4}O_{2.8-\delta}$	modified Pechini
STF90P	$Sr_{0.9}Ti_{0.6}Fe_{0.4}O_{2.8-\delta}$	modified Pechini

Solid state synthesis

Appropriate amounts of precursors ($SrCO_3$, Fe_2O_3 and La_2O_3 for LSF, $SrCO_3$, Fe_2O_3 and TiO_2 for STF) were weighed to receive 4 grams (LSF) or 6 grams (STF) of product, ball milled in ethanol for 1 h, then dried at 70 °C. The obtained powders were homogenised in a mortar and subsequently calcined in a Pt crucible. The calcined powders were then reground in a mortar and sintered in air in a Pt crucible. Calcination and sintering parameters are presented in table 3.3.

Table 3.3: Parameters for calcination and sintering

Sample	Calcination		Sintering	
	T (°C)	t (h)	T (°C)	t (h)
LSF6040	1200	1.5	1250	5
LSF57.540*	1000	3	1200|1300	5|5
LSF5040	1200	1.5	1250	5
STF100	1200	2	1350	5
STF97	1200	2	1350	5
STF95	1200	2	1350	10
STF93	1200	2	1350	10

*sample sintered twice

Modified Pechini synthesis

Two solutions were prepared. For solution 1, titanium(IV)-butoxide was added dropwise to an excess of ethanol (~30 ml) while stirring. Solution 2 consisted of citric acid (2 fold molar excess with respect to all cations of the perovskite), $Sr(NO_3)_2$, the Fe-solution and an excess of distilled water (~80 ml). While stirring constantly, solution 1 was slowly added to solution 2. Then the mixture was heated until the evaporation of solvent and subsequent self-ignition. The resulting product was homogenised in a mortar and calcined in air at 1050 °C for 5 h. The calcined powder was reground in a mortar and sintered in air at 1350 °C for 5 h.

Modified Pechini synthesis number 2

Two solutions were prepared. For solution 1 titanium(IV)-butoxide was added drop-wise to a solution of citric acid (citric acid : cations in perovskite = 1:1 (n/n)) in 69 ml distilled water while stirring. Solution 2 consisted of $Sr(NO_3)_2$, $Fe(NO_3)_3 \cdot 9\,H_2O$ and an excess of distilled water (~93 ml). While stirring constantly, solution 1 was slowly added to solution 2. The resulting mixture was stirred at 80 °C for 3 h followed by 150 °C for 6 h. Then it was heated until all solvent had evaporated. The obtained mixture was further heated until spontaneous self-ignition. The resulting product was homogenised in a mortar and subsequently calcined at 1050 °C for 5 h in air. The calcined powder was reground in a mortar and sintered at 1300 °C under O_2 for 12 h.

3.2.2 Targets for the pulsed laser deposition

Stoichiometric as well as 3 %, 5 % and 7 % A-site deficient STF targets for the preparation of thin film samples were prepared *via* solid state synthesis. Appropriate amounts of precursors ($SrCO_3$, Fe_2O_3 and TiO_2) were weighed to receive 9 grams of product, ball milled in ethanol for 1 h, then dried at 70 °C. The obtained powders were homogenised in a mortar and subsequently calcined in a Pt crucible at 1150 °C for 3 h. The calcined powders were then reground in a mortar, uni-axially pressed into pellets with a 30 mm diameter die and a force of 15 tons. Pellets were sintered at 1350 °C for 5 h in air. Before the first ablation, target surfaces were ground with sanding paper, then cleaned with ethanol.

3.2.3 Thin film samples

PLD-derived thin films can be fabricated with higher A-site deficiency, compared to bulk samples, e.g. shown for $SrTiO_3$ [28]. Moreover, they are well suited for model studies of the oxygen exchange kinetics of the materials [29]. Thus, STF thin film samples were prepared in addition to the powder samples. Samples consisted of the YSZ (100) single crystal (polished on side) as electrolyte with a porous Pt/Gd:CeO_2 (GDC) counter electrode on the unpolished side. On the polished side, a dense STF film with varying sub-stoichiometry was used as the working electrode. Between STF thin film and YSZ single crystal, a Pt grid acted as a current collector. Some samples featured an additional ZrO_2 capping layer above the STF film to prevent oxygen exchange with the atmosphere. Capped samples were deposited on 5 mm x 5 mm x 0.5 mm single crystals. Uncapped samples were deposited on 10 mm x 10 mm x 0.5 mm single crystals, then cleaved into six evenly sized pieces. A schematic of the sample geometry is presented in fig. 3.1. A list of all thin film samples is presented in table 3.4.

Table 3.4: Overview of the prepared thin film samples

Name	Stochiometry	Capped/uncapped
STF100TF$_C$	$SrTi_{0.6}Fe_{0.4}O_{2.8-\delta}$	capped
STF97TF$_C$	$Sr_{0.97}Ti_{0.6}Fe_{0.4}O_{2.8-\delta}$	capped
STF95TF$_C$	$Sr_{0.95}Ti_{0.6}Fe_{0.4}O_{2.8-\delta}$	capped
STF100TF	$SrTi_{0.6}Fe_{0.4}O_{2.8-\delta}$	uncapped
STF97TF	$Sr_{0.97}Ti_{0.6}Fe_{0.4}O_{2.8-\delta}$	uncapped
STF93TF	$Sr_{0.93}Ti_{0.6}Fe_{0.4}O_{2.8-\delta}$	uncapped

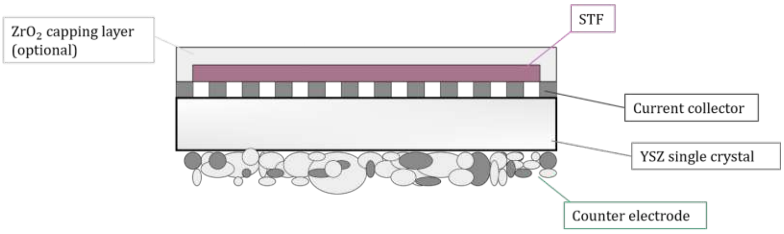

Figure 3.1: Schematic of the thin film samples

Porous counter electrode

Porous counter electrodes were fabricated by spin coating. First, a GDC paste (GDC : ink vehicle = 1:1 (m/m)) was applied onto the unpolished side of the YSZ single crystal *via* spin coating (6000 rpm, 2 min) and dried in the oven. This was followed by a Pt/GDC paste (75 w% Pt, 25 w% GDC, Inc Vehicle) also applied *via* spin coating (6000 rpm, 2 min) and dried in the oven. Finally, as a current collector, a Pt paste was applied with a brush. The counter electrodes were sintered at 1150 °C for 3 h in air.

Pt current collector

The Pt grid was prepared *via* a combination of sputtering, photolithography and ion beam etching. First, a 5 nm Ti layer followed by a 100 nm Pt layer was sputtered on the polished side of the YSZ single crystal. The corresponding parameters are presented in table 3.5. As a next step, the Pt layer was coated with roughly 2 micrometers of photoresist (ma-N-1420 MicroResist Technology) with a spincoater (SCC-200 KLM). The photoresist was baked at 100 °C on a hotplate for 2 min, covered with a shadow mask (square grid with 5 μm wide stripes and holes of 15x15 μm^2) for fine structuring, then crosslinked with UV light (350 W, USHIO 350DP Hg, Ushio, Japan) for 40 s. Subsequently, the sample was developed in a developing solution (ma-D 533s, MicroResist Technology) for 70 s and cleaned with distilled water. Finally, the Pt layer not protect by the photoresist was removed *via* ion beam etching. The corresponding parameter are presented in table 3.6. The samples were then cleaned with ethanol to remove the remaining photoresist. The whole process is sketched in fig. 3.2

Table 3.5: Parameters for the sputtering of Ti and Pt

	Ti	Pt
Sputter time (s)	56	161
Argon pressure (mbar)	$7.3 \cdot 10^{-3}$	$2 \cdot 10^{-2}$
Sputter current (mA)	100	100
Presputter time (s)	30	30
Target to substrate distance (cm)	6	6
Desired film thickness (nm)	5	100

Table 3.6: Parameters for the ion beam etching

Etching time (min)	12
Argon pressure (mbar)	$9 \cdot 10^{-4}$
Plasma current (mA)	15
Beam voltage (V)	400
Accelerator voltage (V)	80

Pulsed laser deposition

After preparing the counter electrode and the current collector, STF thin films were deposited above the current collector using PLD. To that end, target and sample were placed inside a vacuum chamber, at a distance of 6 cm. To allow for contacting of the current collector later on, small parts of the sample surface were covered either with a ZrO_2 paste or by the sample holder. The chamber was evacuated to $\leq 10^{-4}$ mbar, then the pressure was adjusted using O_2. The target was ablated with a KrF excimer laser (Complex Pro 201F) with a wavelength of 248 nm. Parameters are presented in table 3.7. Target and sample were rotated during the ablation to ensure an even layer deposition. For this, the new PLD chamber of the Fleig group was used. Compared to the standard conditions, the target surface was lifted 7 mm above the standard height, the laser lens working distance was increased from 91 to 101 mm in order to achieve the "standard" spot size on the higher target. The substrate was placed in the center of the rotating assembly and rotated with roughly 4 rpm during deposition. Before each deposition, targets were pre-ablated with 10 Hz for 30 s. For some samples, film thickness was estimated with a quartz microbalance.

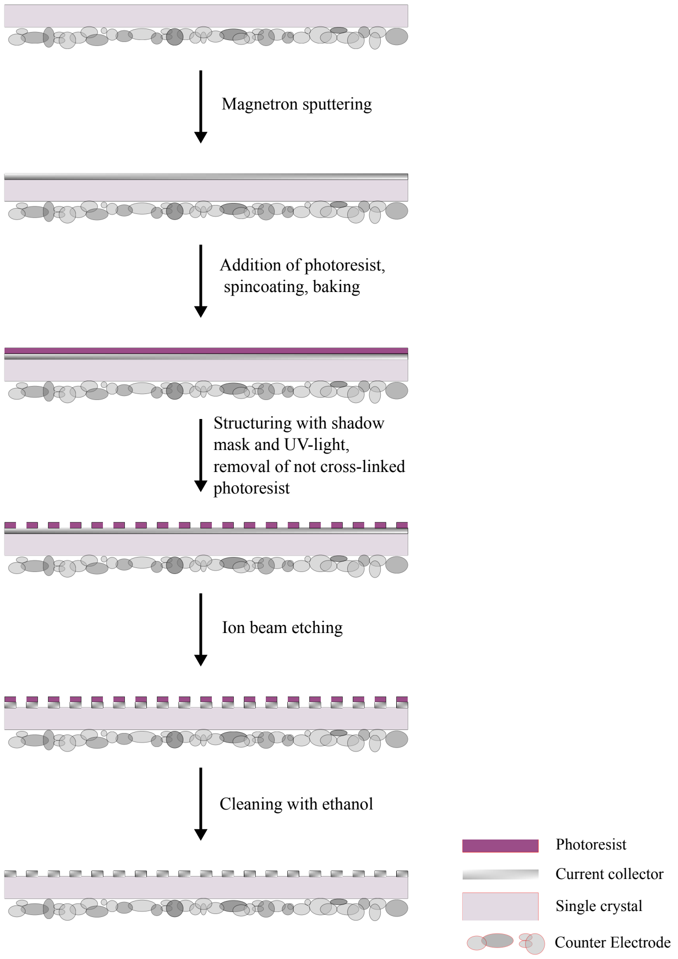

FIGURE 3.2: Workflow for the preparation of the current collector grid

TABLE 3.7: PLD parameters for the deposition of STF

Heating power (%)	52
Temperature (°C)	650
Number of pulses	18000
Frequency (Hz)	10
Time (min)	30
Pressure (mbar)	$4 \cdot 10^{-2}$
Energy set (mJ)	400
Cooling rate (K/min)	15

3.3 Chemical analysis

3.3.1 Inductively coupled plasma mass spectrometry

ICP-MS was performed to determine the stoichiometry of powder samples. About 5 mg of each powder were dissolved in a combination of 2.5 ml HCl and 60 μl HF (the HF aids in complexing the Ti ions), heated in a ~100 °C water bath for 6 h, then left at room temperature over night. At this point, incomplete dissolution of the powder was noticeable for some samples. Sample solutions were then diluted in a mixture of deionised water obtained by Barnstead™ Easypure™ II (18.2 MΩcm) 1 vol% HNO_3 (conc.) and 1 ppb In to yield a final sample concentration of 1-10 ppb. Measurements were performed with a Thermo Scientific™ iCAP™ TQe ICP-MS system (Thermo Fisher Scientific, Bremen, Germany). ICP multi-element standard solution VIII (Certipure®, Merck, Germany) and 1000 mg/kg Ti single element standard (Certipure®, Merck, Germany) were used as an internal standard. The measurement conditions are presented in table 3.8.

Table 3.8: Parameters for the ICP-MS measurements.

Plasma power (W)	1550
Dwell time (s)	0.1
Nebulizer gas (Ar) flow (l/min)	1
Coolgas (Ar) flow (l/min)	14
Auxiliary gas (Ar) flow (l/min)	0.8
Collision gas (O_2) flow (ml/min)	0.33
Measured isotopes (as oxides)	^{46}Ti, ^{47}Ti, ^{48}Ti, ^{54}Fe, ^{56}Fe, ^{86}Sr, ^{88}Sr, ^{115}In

3.4 Structural characterization

3.4.1 Scanning electron microscopy

Scanning Electron Microscope (SEM) measurements of thin films to inspect sample morphology and film thickness were performed with a FEI Quanta 250 FEGSEM at USTEM (TU Wien). Sample morphologies were inspected with a Secondary Electron (SE) detector in top view. Additionally, film thicknesses were measured on cross sections. Here, Backscattered Electron

(BSE) measurements were performed to aid in differentiating between different layers. 5 nm Au/Pd were sputtered on cross section and capped thin films to provide the necessary conductivity. Uncapped thin films were grounded *via* the current collector.

3.4.2 X-Ray diffraction

To check for successful synthesis and phase purity, X-Ray Diffraction (XRD) measurements were performed using a Panalytical XPert PRO diffractometer with para-focussing Bragg-Brentano arrangement, equipped with a Cu tube and XCelerator detector. Scans were performed from $2\Theta = 10°$ to $2\Theta = 90°$. Panalytic Highscore was used evaluate the diffractograms.

3.5 Electrochemical characteriztation

3.5.1 Coulometry of powders

Coulometry of powders was performed to assess the change of oxygen stoichiometry of the samples with varying pO_2.

Setup

Coulometry was performed inside titration cells (roughly 1 cm x 1 cm x 0.5 cm) built out of two seperate electrochemical cells based on two sintered polycrystalline YSZ electrolyte pellets stacked on top of each other. The bottom cell acted as a Nernst sensor to measure the oxygen partial pressure, while the top cell was used for electrochemical pumping of oxygen. A schematic is depicted in fig. 3.3. The bottom cell consisted of an YSZ cup as electrolyte coated with Pt electrodes on both sides. The top cell consisted of an YSZ plate as electrolyte and $Pr:CeO_2$ (PCO) nanopowder electrodes with a Pt current collector on both sides. The electrodes and current collectors were applied with a brush, contacted with Pt wires and sintered at 1000 °C for 3 h. The sample was filled into the bottom cell, then covered with the top cell. Glass ceramic foil (KeraGlas ST K03) placed in between top and bottom cell was used to seal the two cells gas-tight. The titration cell was placed inside a high-temperature measuring chamber consisting of alumina and fused silica and a mild force of ca 2 Newton was applied to hold the cell in place and assist the sealing process. Inside, it was contacted with Pt sheets and wires.

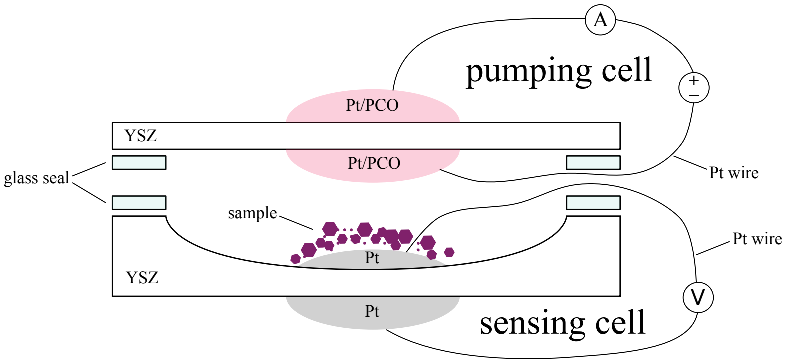

Figure 3.3: Schematic of the titration cell for the coulometry of powder samples.

The chamber was placed inside a tube furnace. The setup is shown in fig. 3.4. To seal the titration cell gas tight, it was first slowly heated to 500 °C (2 °C/min) in order to calcine organic compounds in the glass ceramic foil. Then the titration cell was quickly heated to 850 °C (10 °C/min) and held there for 1 h to join the glass seals together.

Figure 3.4: The used measurement setup for the coulometry of powders.

Measurement

Coulometry of powders was performed in galvanostatic mode at 625 °C. First, oxygen was pumped into or out of the setup *via* the top cell (pumping cell) during a constant current step. This was followed by an open circuit step during which the cell potential was monitored *via* the bottom cell (sensing cell). A schematic of the resulting current and voltage curves is presented in fig. 3.5. Measurements usually consisted of two alternating reductive and oxidative half cycles. The pO_2 inside the setup was reduced stepwise until the sensing cell reached a potential of around -1.2 V (corresponding to a pO_2 of about 10^{-28} bar inside). Afterwards, the O_2 was

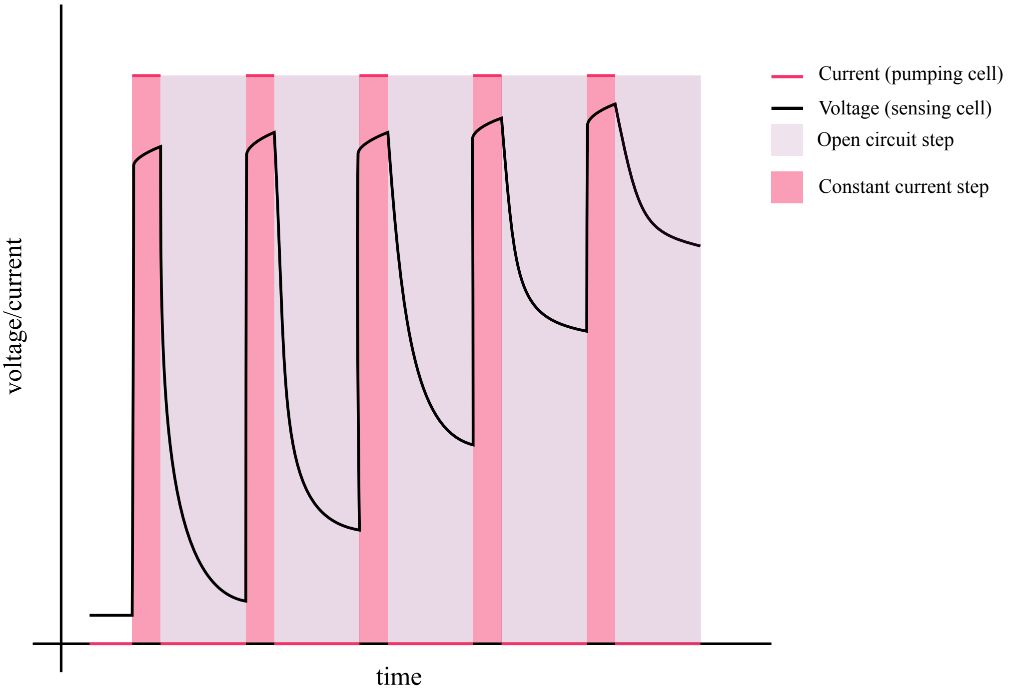

Figure 3.5: Schematic of the resulting current and voltage curves in galvanostatic mode for a oxidative half cycle.

stepwise pumped back into the cell until the sensing cell reached a potential of around 0.03 V (corresponding to a pO_2 of about 1 bar inside). Then the half cycles were repeated once or twice. Constant current steps were held between 30 s to 60 s, open circuit steps for 10 min or until the change of voltage at the sensing cell was below 1 mV per minute. The applied current normally ranged from 0.1 mA to 1 mA. Resulting potentials at the pumping cell lay in between -2.5 V to 1 V. Sample amounts usually ranged from 10 mg to 30 mg.

3.5.2 Coupled coulometry and electrochemical impedance spectroscopy

Capped thin film samples were analysed *via* coulometry and EIS simultaneously to assess changes of the samples oxygen stoichiometry and chemical capacitance with varying pO_2 as well as to compare both methods. For a combined measurement, first an impedance spectrum was recorded. This was followed by a linear voltage sweep to a new potential during which the current was recorded. After the resulting current spike had relaxed and the current had

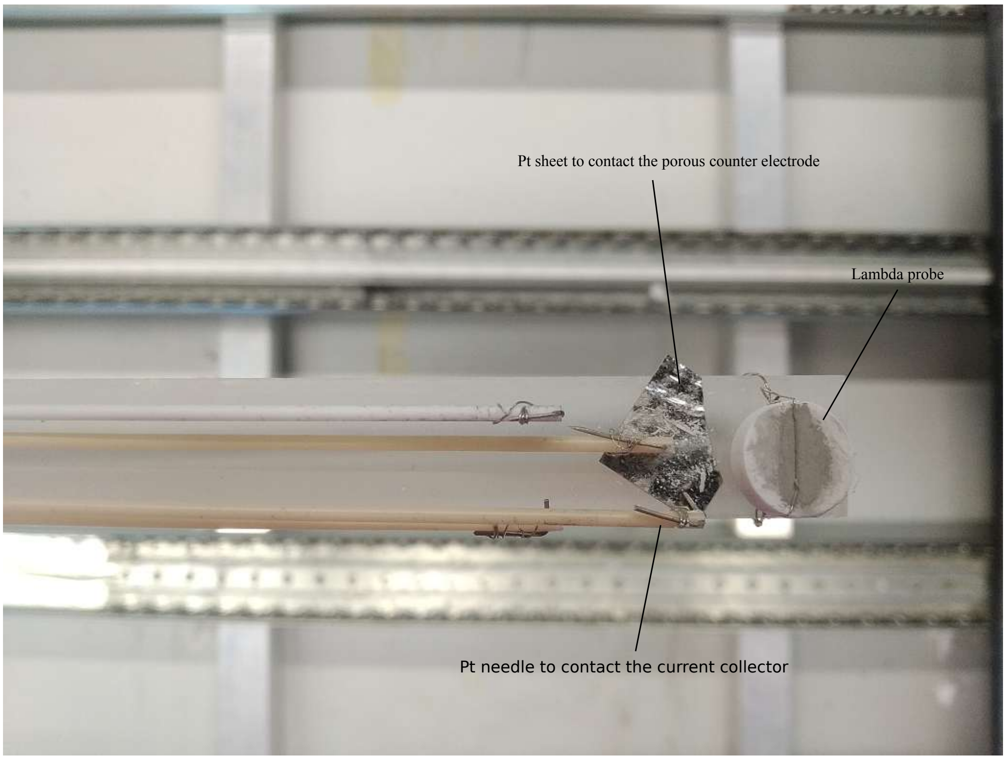

Figure 3.6: The measurement setup used to analyse thin film samples

converged to a constant value a new impedance spectrum was started. Then the cycle was repeated. A schematic of the applied voltage curves and the resulting current curves is presented in fig. 3.7.

Setup

Measurements on thin films were performed inside a Al_2O_3 measuring sword covered with a quartz glass cylinder, then placed inside a tube furnace. The samples were placed on a Pt sheet to contact the porous counter electrodes. The current collectors and thus the thin films were contacted with a Pt needle. A lambda probe fabricated from a used coulometry titration cell filled with Fe and FeO was used to monitor the pO_2 in the surrounding atmosphere. The measurement setup is depicted in fig. 3.6.

Coulometry

Coulometry of capped thin films was performed to assess the change of oxygen stochiometry of the samples with varying pO_2. Measurements were performed in potentiostatic mode. First, a constant voltage was applied and the resulting current monitored. Here, the current converged to a constant leakage current due to reactions of the thin film with the surrounding O_2 despite the zirconia capping layer. Then, the voltage was gradually changed until the next desired voltage was reached and a new constant voltage step was started. The bias voltage ranged from 0.2 V to -1.6 V against N_2 with a step size of 20 mV. Constant voltage steps were held for 30 - 120 s, depending on the speed of equilibration (long steps at high and low pO_2, short steps at intermediate pO_2). The applied voltage was changed with a rate of 10 mV/s over the course of 2 s. Each measurement started with a reductive half cycle, stepwise decreasing the bias voltage to the chosen minimum value. This was followed by an oxidative half cycle, stepwise increasing the bias voltage to the chosen maximum value. Reductive and oxidative half cycles were repeated once before changing the lower bound of the bias voltage. Measurements were conducted under N_2 in order to reduce the leakage current through the ZrO_2 layer. The residual oxygen partial pressure of ~10 ppm was monitored with a coulometric titration cell filled with a Fe/FeO mixture that delivers a constant reference pO_2. A schematic of the resulting current and voltage curve is presented in fig. 3.7

Electrochemical impedance spectroscopy

Impedance spectroscopy measurements of capped thin films at varying bias voltage were performed with a Bio-logic SP-200 potentiostat. Spectra were recorded at the end of each constant voltage step of the coulometry as shown in fig. 3.7. Measurements were usually performed between 10 kHz and 20 mHz with an amplitude of 10 mV.

3.5.3 Electrochemical impedance spectroscopy of uncapped thin films

EIS was performed on uncapped thin film samples under oxidising conditions (pO_2 of 0.21 bar) and reducing conditions ($6 \cdot 10^{-24}$ bar) at 625 °C to study oxygen exchange kinetics. All samples were simultaneously placed inside a Al_2O_3 measuring sword covered with a quartz glass cylinder, then placed inside a tube furnace and alternatingly measured by a multiplexing setup. The samples were placed on a Pt sheet to contact the porous counter electrodes. The current collectors and thus the thin films were contacted with Pt needles. The measurement setup is

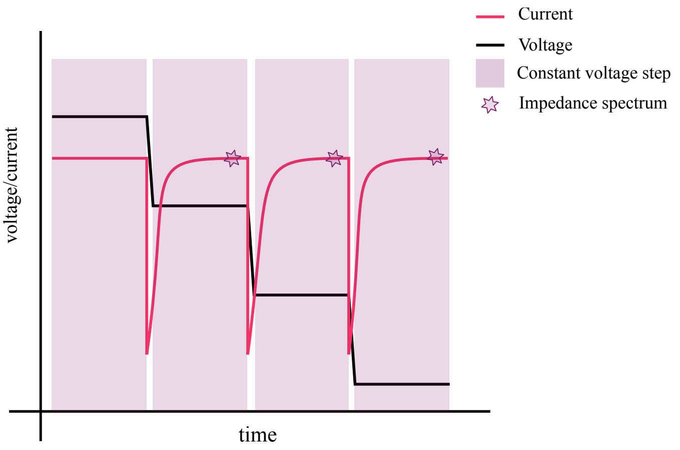

Figure 3.7: Schematic of the resulting current and voltage curves in potentiostatic mode

depicted in fig. 3.6. Measurements were performed between 10 MHz and 20 mHz with an amplitude of 10 mV. The variation of oxygen partial pressure was achieved by mixing N_2, humidified H_2 in Argon and O_2 in varying ratios. Measurements were first performed under oxidising conditions, then reducing conditions. This was again followed by measurements under oxidising conditions, then reducing conditions. Between changes of the atmosphere, the setup was purged with N_2 for 300 min. At each atmosphere step all samples were measured consecutively 10 times. After each set of measurements, the setup was flushed with the corresponding gas mixture for 20 min.

3.6 Additional analysis

3.6.1 X-ray photoelectron spectroscopy (XPS)

Sample preparation

Transition metal oxidation states were measured by means of XPS on electrochemical model cells with thin film STF working electrodes. For this purpose, appropriate substrates with an oxygen ion buffering counter electrode were fabricated as follows: 80 w% GDC and 20 w% Fe_2O_3 were dispersed in ink vehicle in a 1:1 weight ratio and homogenized in a rotary ball mill (Fritsch pulverisette). The paste was spin-coated on the unpolished side of 10x10x0.5 mm^3 (100) oriented single-crystalline YSZ substrate at a speed of 2400 rpm, and dried. After application of a thin layer of Pt paste, the counter electrode was sintered at 1050 °C for 3 h in air. Thin

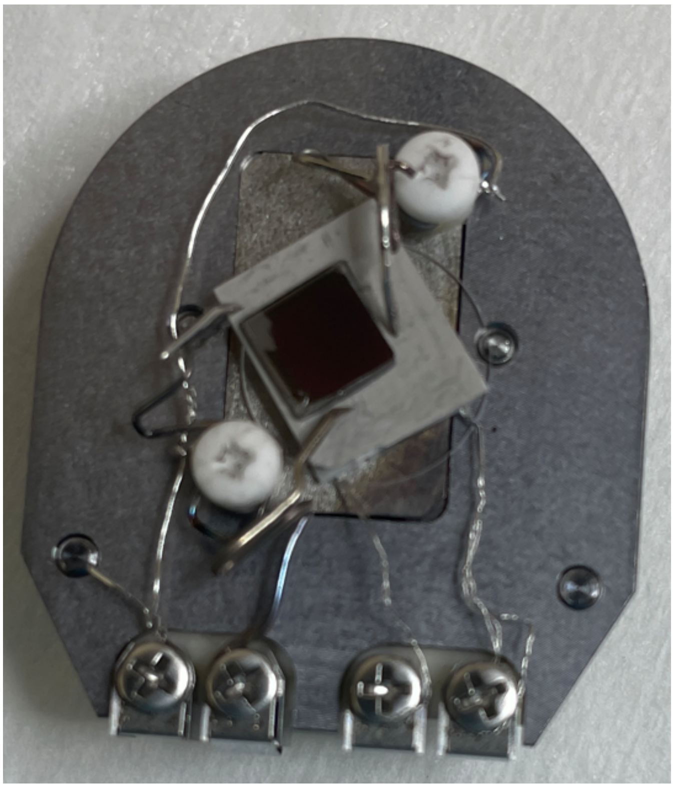

Figure 3.8: Model cell with STF100 working electrode mounted and contacted on the PHI versa probe sample holder with four electrical contacts.

film platinum current collectors and STF100, as well as STF95 films were deposited on these substrates with the same parameters as used for the STF thin films described in section 3.2.3, and the substrates were cleaved in four pieces of approximately 5mm x 5 mm x 0.5 mm

Setup and Measurement

The resulting cells were mounted in a PHI VersaProbe 4 XPS spectrometer on a heated stage with electrical contacts for working and counter electrode. The X-ray source was a monocromated Al K_α source operating at 50 W. The thin-film working electrode was kept at ground potential, while the electrochemical polarization was applied to the counter electrode by means of a Bio-logic SP-200 potentiostat. During XPS measurements, the temperature was controlled through the known conductivity-temperature relationship of YSZ [30]. A picture of the sample mounted on the sample holder is shown in fig. 3.8.

For controlled oxygen activity in the working electrode, constant and known counter electrode oxygen activity is important. For this purpose, the sample was heated in the XPS chamber to ca 400 °C, and a constant current of +50 µA was applied to the cell for 2000 s, in order to release O_2 through the working electrode. During this time, the Fe_2O_3 phase of the counter electrode was partially reduced to Fe metal. By this means, the counter electrode oxygen activity was fixed to that of the Fe/FeO phase equilibrium with

$$a(O_2)_{\text{counter electrode}} = e^{\frac{2\,\Delta_f G^\circ}{RT}}, \tag{3.1}$$

where $a(O_2)_{\text{counter electrode}}$ is the oxygen activity at the counter electrode and $\Delta_f G^\circ$ the molar standard formation enthalpy of FeO in $\frac{J}{mol}$, which was taken from [31] as

$$\Delta_f G^\circ = -303097 + 683.498T - 91.3978T\mathit{ln}\frac{T}{K} + 0.05180T^2. \tag{3.2}$$

Therein the units of the experimentally determined coefficients are $\frac{J}{mol}$, $\frac{J}{mol \cdot K}$, $\frac{J}{mol \cdot K}$ and $\frac{J}{mol \cdot K^2}$ respectively.

The accuracy of the values in this publication was confirmed by the self-fabricated single-chamber lambda probe, described in section 3.5.2. Consequently, the oxygen activity in the working electrode can be determined from the cell voltage according to Nernst's equation by

$$a(O_2)_{\text{working electrode}} = e^{\frac{2\Delta_f G^\circ + 4F \cdot E_{\text{cell}}}{RT}}, \tag{3.3}$$

where $a(O_2)_{\text{working electrode}}$ is the oxygen activity at the working electrode and E_{cell} the applied cell voltage.

A similar cell design with an oxygen sub-stoichiometric GDC counter electrode [32] was used already in a previous publication. Here, however, the new counter electrode design allows for a much better control of the oxygen activity. After the initial partial reduction of the counter electrode, various voltages were applied to the cell, and XPS spectra were acquired with an analyser pass energy of 55 eV (for the broader Fe 2p, Fe 3p and O 1s transitions) and 27 eV (for the narrower Sr 3d and Ti 2p).

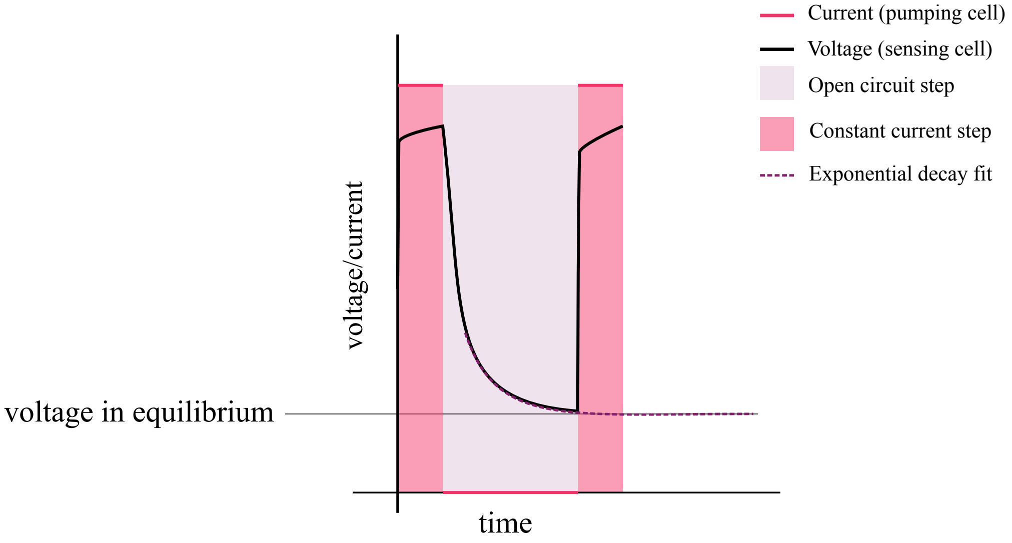

Figure 3.9: Schematic of the interpretation of the voltage curves in galvanostatic mode

3.7 Data evaluation

3.7.1 Coulometry of powders

Data from the galvanostatic coulometry consisted of a charge step and a relaxation step. A sketch of the resulting potential and current curves is presented in fig. 3.9. If the voltage had not reached a constant value at the end of each open circuit step, an exponential fit was used to estimate the voltage in equilibrium. As a next step, the corresponding pO_2 inside the cell was calculated from the determined voltages *via*

$$\mathrm{pO_2}_{\mathrm{inside}} = \mathrm{pO_2}_{\mathrm{outside}} \cdot e^{\frac{4F}{RT} \cdot OCV}. \tag{3.4}$$

Therein $\mathrm{pO_2}_{\mathrm{inside}}$ is the oxygen partial pressure inside the titration cell in bar, $\mathrm{pO_2}_{\mathrm{outside}}$ is the oxygen partial pressure in the surrounding atmosphere (0.21 bar for air) and OCV the measured equilibrium cell voltage in open circuit conditions in V.

The charge transported in each step was corrected for the cell volume and for the electron conductivity of the electrolyte at low pO_2 as described in section 3.7.1. The corrected charge was then used to calculate the change in oxygen stoichiometry of the sample *via*

$$\delta_n = \frac{Q_n}{2\mathrm{F} \cdot \mathrm{n_{sample}}} + \delta_0. \tag{3.5}$$

Here δ_n is the deviation from the oxygen stoichiometry per formula unit at the nth step, Q_n the charge at the nth step in C and n_{sample} the molar amount of the sample inside the titration cell. δ_0 is the oxygen stoichiometry at the start of the experiment. Furthermore, the oxygen non-stoichiometry δ is chosen such that it is zero in the stoichiometry plateau in the intermediate pO_2 range, which corresponds to $O_{2.8}$ for the A:B stoichiometric LSF and STF powders.

A strength of the coulometric titration technique is that phase transitions of easily reducible phases can be detected. Varying oxygen content at a constant oxygen partial pressure is indicative for a phase transition. In the case of Fe containing perovskites, these phase transitions are primarily associated with the reduction of a Fe^{3+} oxide to iron metal. Consequently, three electrons are required per Fe metal atom, so the molar fraction of metallic Fe can be calculated according to

$$x_{phase} = \frac{\Delta Q_{phase}}{3F \cdot n_{sample}}. \tag{3.6}$$

Therein x_{phase} is the molar fraction of the secondary phase, ΔQ_{phase} is the change in charge over the course of the phase change in C and n_{sample} the molar amount of the sample inside the titration cell.

Charge correction

Apart from sample oxygen stoichiometry changes, also gas phase oxygen within the sealed cell (relevant > 10 mbar) and electronic current through the pumping cell electrolyte (relevant at very low oxygen partial pressures) lead to deviations of the observed charge, which must be corrected. The total charge measured can thus be described by

$$Q_{measured} = Q_{sample} + Q_{O_2} + Q_{eon}, \tag{3.7}$$

where $Q_{measured}$ is the charge measured, Q_{sample} the charge attributed to reactions of the sample, Q_{O_2} the charge associated with gas phase O_2 that is removed *via* the pumping cell and Q_{eon} the charge caused by the electron conductivity of the electrolyte.

The charge associated with gas phase O_2 was calculated *via*

$$Q_{O_2} = \frac{4F \cdot V_{cell} \cdot pO_{2inside}}{RT}. \tag{3.8}$$

Here Q_{O_2} is the charge attributed to the O_2 flux associated with the volume of the titration cell, V_{cell} the volume of the titration cell in m^3 (approximately $1.2 \cdot 10^{-8}$ m^3) and $pO_{2_{\text{inside}}}$ the oxygen partial pressure inside the titration cell in bar calculated by eq. ((3.4)).

Contributions due to electron conductivity of the electrolyte were estimated according to

$$Q_{\text{eon}} = \int G_{e^-} \cdot \frac{\text{RT}}{\text{F}} \, dt, \tag{3.9}$$

where Q_{eon} is the charge caused by the electron conductivity of the electrolyte in C. G_{e^-} is the electron conductance of the electrolyte in S calculated according to [33] by the equation

$$G_{\text{e}^-} = 1.31 \cdot 10^{-7} e^{\frac{3.88\,eV}{k_B\,T}} \cdot (\text{pO}_{2_{\text{pump}}})^{-\frac{1}{4}} \cdot \frac{A_{\text{electrode}}}{d_{\text{elctrolyte}}}. \tag{3.10}$$

Therein $A_{\text{electrode}}$ and $d_{\text{elctrolyte}}$ are the area covered by the electrode in cm^2 and the thickness of the electrolyte in cm respectively. The unit of the experimentally determined coefficient is $\frac{S\,bar^{\frac{1}{4}}}{cm}$. $pO_{2_{\text{pump}}}$ is the resulting pO_2 at the electrode due to the applied potential in bar, which was calculated *via*

$$\text{pO}_{2_{\text{pump}}} = \text{pO}_{2_{\text{outside}}} \cdot e^{\frac{4F}{RT} \cdot E - (R_{\text{electrolyte}} - R_{\text{airelectrode}}) \cdot I}. \tag{3.11}$$

Here $pO_{2_{\text{outside}}}$ is the pO_2 in the surrounding atmosphere (0.21 bar for air). $R_{\text{airelectrode}}$ is the polarisation resistance of the electrode on the outside of the pumping cell, which was estimated.

Due to the imperfect electrode and electrolyte geometry, the electrode area and separation can only be estimated. Consequently these were not determined from the geometry, but rather chosen so that subsequent oxidation and reduction half cycles appeared reversible. Noteworthy, electronic leakage is only an issue in very reducing conditions that correspond to almost dry hydrogen. Moreover, the major portion of the electronic leakage stems from the pumping cell during the galvanostatic step, where the inner pumping electrode overpotential induces a very low $pO_{2_{\text{pump}}}$.

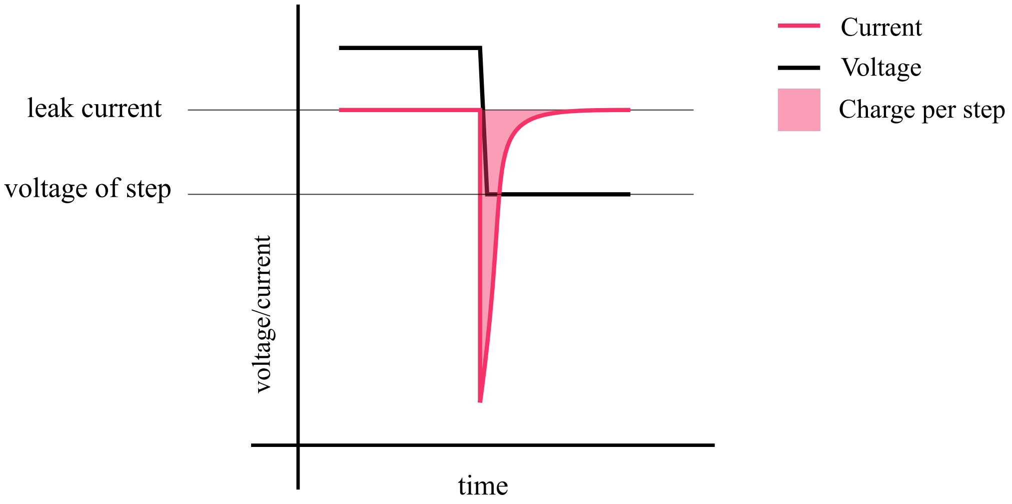

Figure 3.10: Schematic of the interpretation of the current curves in potentiostatic mode

3.7.2 Coupled coulometry and electrochemical impedance spectroscopy of capped thin films

Coulometry

In contrast to the coulometric titration cells, leakage currents that do not correspond to oxygen stoichiometry changes are much larger for thin-film based cells, and they are in large parts not due to electron conduction through YSZ, but stem from reactions with the surrounding O_2. Consequently, the leakage current correction is much more important here. Data from the potentiostatic coulometry consisted of a capacitive current spike at changing potential, followed by relaxation to a constant current value before the next change in potential. Each current spike was numerically integrated to yield the corresponding charge transferred at each voltage step according to

$$\Delta Q_{\text{step}} = \int_{\text{begin step}}^{\text{constant current}} I - I_{leak} \,\mathrm{d}t. \tag{3.12}$$

Therein ΔQ_{step} is the charge of the analysed step in C. I and I_{leak} the current and leakage current in A respectively. The leakage current was estimated *via* an exponential decay fit of the measured current of each step. A sketch is presented in fig. 3.10.

The oxygen non-stoichiometry was further calculated according to

$$\delta_n = \frac{\sum_{i=1}^{n} \Delta Q_{\text{step}_i}}{2\text{F} \cdot \text{n}_{\text{sample}}} + \delta_0. \tag{3.13}$$

Here δ_n is the deviation from the oxygen stoichiometry at the n^{th} step per formula unit, ΔQ_{step_i} the charge at the i^{th} step in C and n_{sample} the molar amount of the sample inside the titration cell. δ_0 is the oxygen stoichiometry at the start of the experiment. Furthermore, the oxygen non-stoichiometry δ is chosen so that it is zero at the stoichiometry plateau in the intermediate pO_2 range, which corresponds to $O_{2.8}$ for the A:B stoichiometric powders.

For each voltage step, the corresponding nominal pO_2 (denoted as oxygen activity $a(O_2)$) was calculated using eq. ((3.4)). Additionally, the chemical capacitance at each voltage step was calculated by

$$C_{\text{chem,dc}} = \frac{\Delta Q_{\text{step}}}{\Delta E_{\text{step}}}. \tag{3.14}$$

Therein $C_{\text{chem,dc}}$ is the chemical capacitance in F, ΔQ_{step} the change in charge for the analysed step in C (from eq. ((3.12))) and ΔE_{step} the change in voltage per step in V.

Electrochemical impedance spectroscopy

Electrochemical impedance spectra were fitted with ZView4®. The equivalent circuit used to fit the capped samples is given in fig. 3.11. The high frequency intercept was identified as a combination of the ionic transport resistance of the YSZ single crystal, the resistance of the current collector and the resistance of the wiring. The semi-circle at intermediate frequencies was attributed to the counter electrode. Since neither the electrolyte nor the counter electrode resistance were of interest in this work, the fit range was limited to the capacitor-like low-frequency feature. Consequently, the sum of the high frequency intercept and the feature ascribed to the counter electrode were fitted to one resistance. The low frequency feature was interpreted as a combination of the ZrO_2 capping layer and the chemical capacitance of the thin film. It was fitted to a R/Constant Phase Element (CPE) element. Whenever the associated capacitance was too large to reliably determine the resistance of the capping layer a R/C

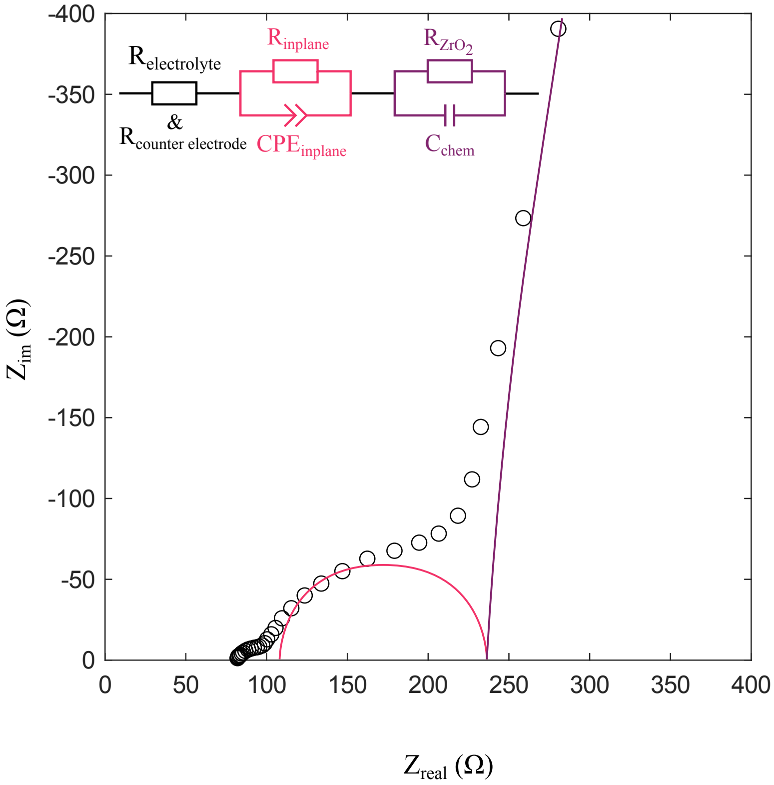

Figure 3.11: Exemplary impedance spectrum and corresponding equivalent circuit for the capped thin film samples. Coloured lines schematically show, which parts of the equivalent circuit represent which part of the impedance response.

element was chosen to fit the low frequency feature instead, in order to be able to accurately determine the sample capacitance. The corresponding capacitance of the R/CPE element was calculated *via*

$$C_{\mathrm{CPE}} = \frac{(R_{\text{capping layer}} \cdot T_{\mathrm{CPE}})^{P_{\mathrm{CPE}}^{-1}}}{R_{\text{capping layer}}}, \tag{3.15}$$

where eq. ((3.15)) C_{CPE} is the calculated capacitance of the R/CPE element, $R_{\text{capping layer}}$ the resistance of the capping layer, P_{CPE} the dimensionless CPE exponent and T_{CPE} the CPE parameter.

In some spectra, an additional feature was visible at a frequency range between the feature attributed to the counter electrode and the low frequency feature attributed to the thin film and capping layer. This is assumed to stem from the in-plane ionic transport resistance of the thin films, which is more dominant due to the non-ideal current collectors shown in section 4.3.1. The chemical capacitance of the thin films determined for each voltage step was used to calculate the corresponding charge *via*

$$\Delta Q_{\text{step}} = C_{\text{chem}} \cdot \Delta E_{\text{step}}. \tag{3.16}$$

Here eq. ((3.16)) C_{chem} is the chemical capacitance (C_{CPE} from eq. ((3.15))) in F, ΔQ_{step} the change in charge for the analysed step in C and ΔE_{step} the change in voltage in V.

This charge per step was then used to calculate the change in oxygen stoichiometry using eq. ((3.5)).

3.7.3 X-ray photoelectron spectroscopy

XPS measurements were performed to study surface chemistry and to validate the coulometry measurements. Spectra were evaluated by Casa XPS software. The oxygen stoichiometry of the thin film cells was determined by the same method as used for the capped thin films (section 3.7.2). The reactive leakage current in the coulomtery measurements could be neglected however, as a consequence of the negligible atmospheric pressure. Due to the explorative nature of these first experiments, the oxygen non-stoichiometry of the STF95 sample was determined by the EIS method, whereas the STF100 sample was evaluated by coulometry.

4 Results and Discussion

4.1 $La_{0.6}Sr_{0.4}FeO_{2.8-\delta}$

4.1.1 X-ray diffraction

To assess phase purity, XRD measurements were performed for all synthesised powders. XRD patterns of stoichiometric and sub-stoichiometric LSF are shown in fig. 4.1. All three patterns exhibit a rhombohedral perovskite-type phase. For sub-stoichiometric LSF, however, a secondary phase is visible that was identified as $SrFe_{12}O_{19}$ by comparison with a database. This is in accordance with synchrotron measurements performed on sub-stoichiometric LSF [34]. For stoichiometric LSF, no secondary phase is visible. Additionally, no new reflexes are present after the coulometry and the existing reflexes appear narrower, which is indicative for larger crystallites or higher chemical homogeneity - opposite to what one would expect for the onset of a phase decomposition reaction. This indicates that no irreversible phase change took place during the coulometry above the detection limit of the XRD.

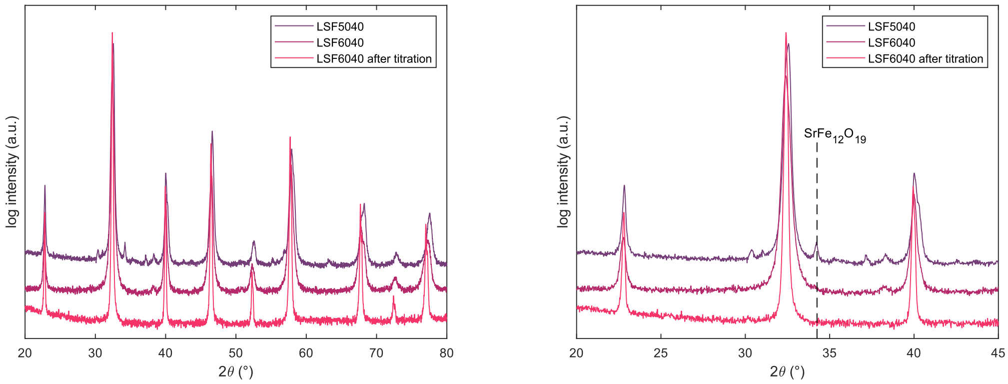

Figure 4.1: XRD patterns of stoichiometric und 10 % sub-stoichiometric LSF. The most dominant peak of the $SrFe_{12}O_{19}$ phase is marked.

4.1.2 Coulometry

Changes of oxygen stoichiometry vs pO_2 of stoichiometric and 2.5 % sub-stoichiometric LSF powder were measured by coulometry, as described in section 3.5.1. 15 - 60 mg of powder were weighed in each titration cell, and coulometry was performed in galvanostatic mode at 625 °C, with 0.24 C per galvanostatic step, corresponding to roughly 0.005 O atoms per formula unit and step. An exemplary plot of the resulting raw data is presented in fig. 4.2. Measurements were evaluated as described in section 3.7.1. The corresponding results are presented in fig. 4.3. Due to limited equilibration kinetics, the titration cell did not converge towards a stable equilibrium voltage for some steps, especially in the oxidative half cycles. These data points were left out in the plot, resulting in some gaps in the plotted data. In the oxygen partial pressure range between 1 and 10^{-24} bar, the oxygen stoichiometry is in line with the literature [23]. At high pO_2, the oxygen content increases and converges towards three per formula unit. At intermediate pO_2, the oxygen content approaches a broad plateau at $O_{2.8}$ per formula unit.

The measurement of the 2.5 % sub-stoichiometric sample appears perfectly reversible, whereas an offset between first and second run is observable for the stoichiometric sample. This offset, however, is most likely caused by electron conductivity of the electrolyte of the measuring cell and does not represent a reaction of the sample. A hysteresis in the intermediate pO_2 range can be observed for both samples. Most likely, this hysteresis is not a thermodynamic property of the samples, but rather a limitation of the experimental method, which relies on equilibration with a surrounding atmosphere. In the intermediate pressure range (roughly 10^{-15} to 10^{-8} bar), neither gas phase O_2 nor H_2 molecules in a H_2 + H_2O mixture are present in a concentration that is sufficient for equilibration within 10 minutes.

Starting at high oxygen partial pressures, the initial decrease in oxygen stoichiometry can be interpreted as the formation of oxygen vacancies, coupled with the filling of electron holes in accordance with eq. ((2.1)). At an oxygen partial pressure between 10^{-7} and 10^{-23} bar, the sample is stable as $La_{0.6}Sr_{0.4}FeO_{2.8}$, with Fe^{3+}, and O^{2-} leading to a plateau of constant stoichiometry. This stoichiometry plateau was chosen as the reference point for the change in oxygen stoichiometry with $\delta = 0$. At lower oxygen partial pressures, the transition from Fe^{3+} to Fe^{2+} starts, leading to a further creation of oxygen vacancies in accordance to eq. ((2.17)). At 10^{-24} bar pO_2, a phase transition (visible as a change of oxygen stoichiometry at constant pO_2) can be observed. For the sub-stoichiometric sample, this can be attributed to the $SrFe_{12}O_{19}$ phase visible in the XRD. The phase transition in the stoichiometric sample, however, indicates the presence of a secondary phase below the detection limit of the XRD, as there is no secondary phase visible in the XRD data of the stoichiometric sample. Comparison with the

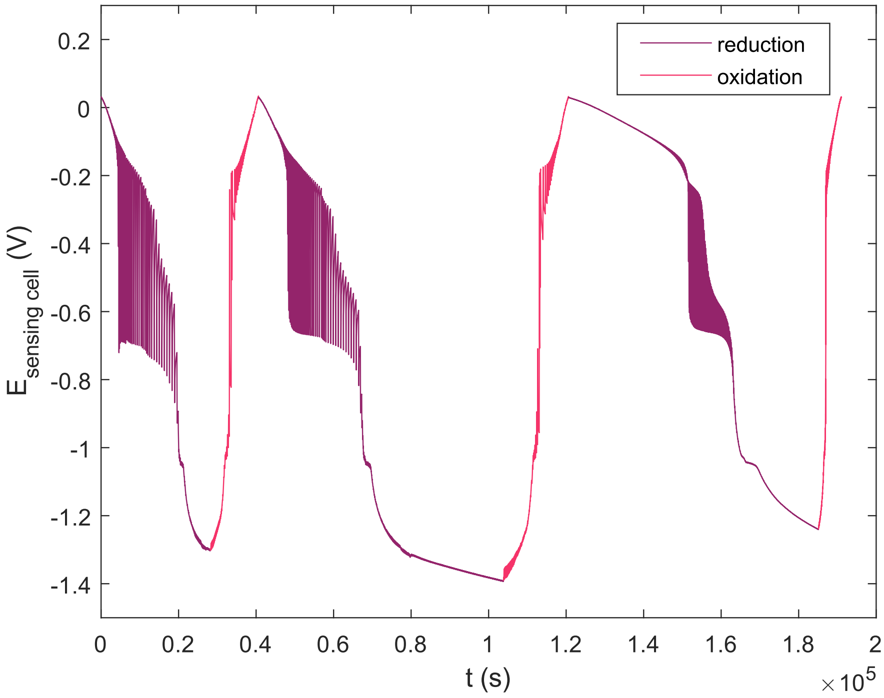

(a) Voltage measured at the sensing cell over time.

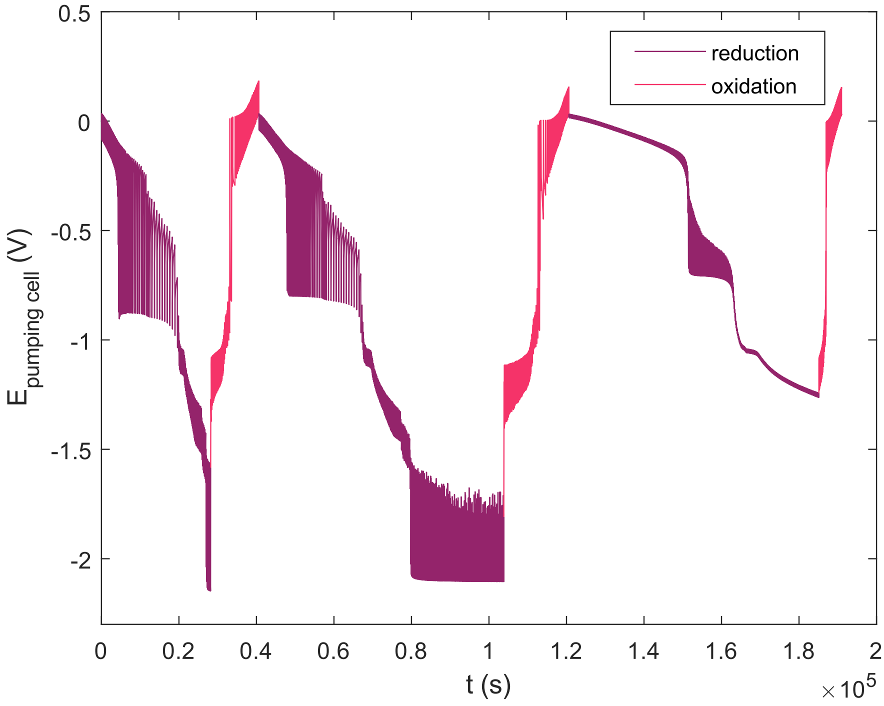

(b) Voltage measured at the pumping cell over time.

Figure 4.2: Exemplary raw data for the coulometry of powder samples. Shown is the measurement of $Sr_{0.97}Ti_{0.6}Fe_{0.4}O_{2.8-\delta}$ prepared *via* the Pechini method.

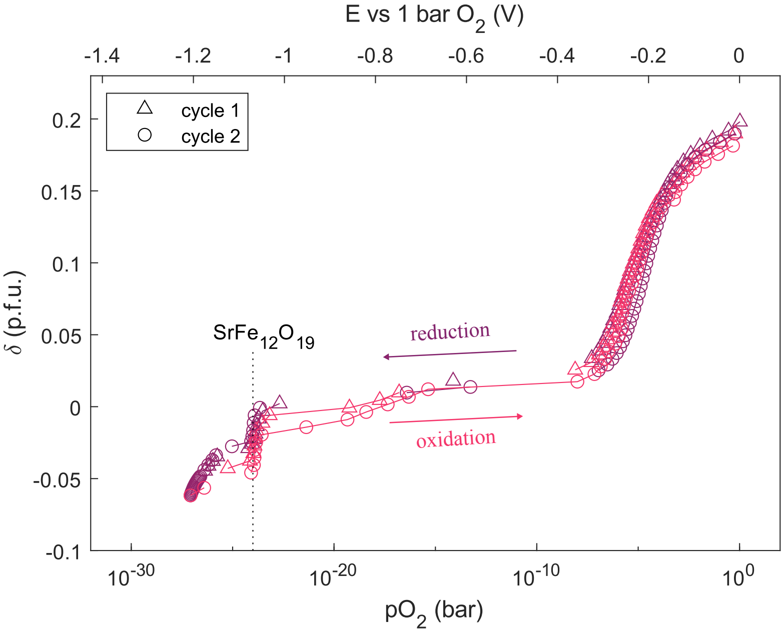

(a) The stoichiometric sample. Calculated amount of Fe in secondary phase: 1.0 %.

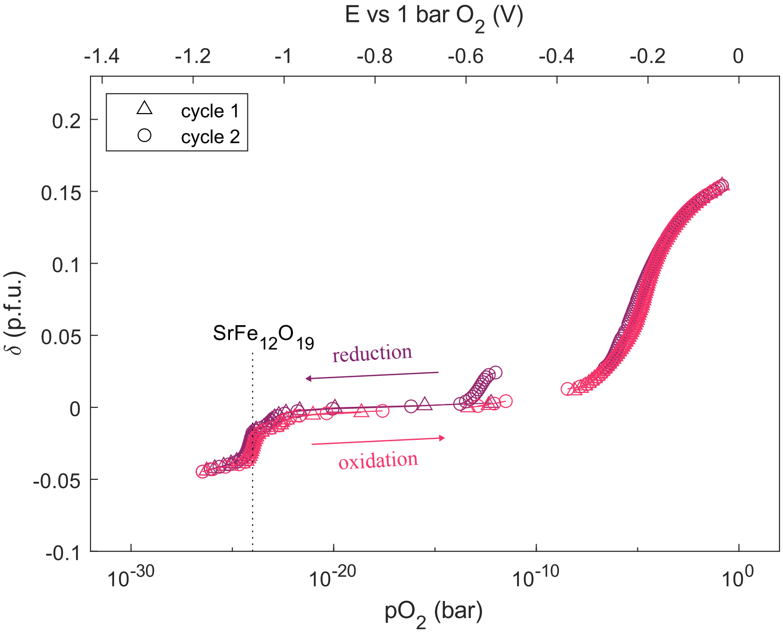

(b) The 2.5 % sub-stoichioemtric sample. Calculated amount of Fe in secondary phase: 1.8 %.

FIGURE 4.3: Change in oxygen stoichiometry vs pO_2 for the stoichiometric and the 2.5 % sub-stoichiometric sample at 625°C. The phase transition is marked.

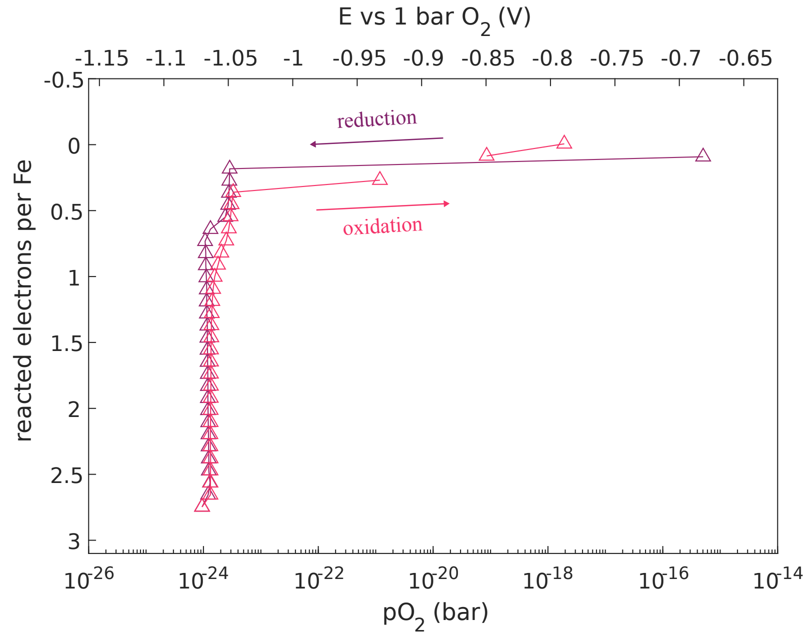

Figure 4.4: Coulometry of Fe_2O_3 showcasing the phase transition of Fe^{2+} to Fe^0 at an pO_2 of 10^{-24} bar.

coulometry of Fe_2O_3 powder fig. 4.4 shows that the phase transition of the samples takes place at the same oxygen partial pressure as the reduction of FeO (transition from Fe^{2+} to Fe^0), which is furthermore in line with literature values [31]. The fact that this phase transition already happens in the first reduction cycle, and appears to be perfectly reversible in subsequent cycles indicates that the phase transition is not the onset of an Fe metal exsolution. In literature, Fe metal exsolution was proven to be irreversible at the given temperature [35]. Additionally, conditions need to be significantly more reducing than the Fe^{2+}/Fe^0 transition to trigger Fe exsolution from a ferrite perovskite lattice [6]. Consequently, such a behavior is indicative for a secondary phase, in which Fe gets reduced to metal. XRD measurements identify the secondary phase as the iron rich phase $SrFe_{12}O_{19}$. Given the very high stoichiometric Fe content, it is likely that the reduction of this phase to Fe metal happens at almost the same $p(O_2)$ as for pure FeO. In conclusion, no phase pure LSF could be synthesized. However, the presented miniature coulometry cell allowed for the detection of the $SrFe_{12}O_{19}$ phase, even if this secondary phase remained invisible in the XRD measurements. Additionally, the percentages of secondary phases were quantified according to section 3.7. Calculated percentages of secondary phases are presented in table 4.1

TABLE 4.1: Calculated amount of Fe in secondary phases for LSF samples ($\frac{n_{(\text{Fe in secondary phase})}}{n_{(\text{LSF})}}$).

Sample	amount of Fe secondary phase (%)
LSF6040	1.0
LSF57.540	1.8

4.2 $SrTi_{0.6}Fe_{0.4}O_{2.8-\delta}$ powder samples

4.2.1 Inductively coupled plasma mass spectrometry

ICP-MS was performed to gain precise sample stoichiometries. The resulting Sr, Ti and Fe contents are presented in table 4.2. Due to problems with the dissolution of the samples, these results are deemed unreliable and are only presented for completeness sake.

TABLE 4.2: Calculated Sr, Ti and Fe content from the ICP-MS.

Name	Sample type	Sr content (%)	Ti content(%)	Fe content(%)
STF100	powder	0.499	0.312	0.189
STF97	powder	0.400	0.402	0.198
STF95	powder	0.417	0.385	0.198
STF93	powder	0.475	0.398	0.127
STF97P	powder	0.504	0.336	0.160
STF95P	powder	0.477	0.374	0.149
STF93P	powder	0.479	0.338	0.183
STF90P	powder	0.470	0.359	0.171

4.2.2 X-ray diffraction

Similarly to LSF, the preparation of phase-pure STF - especially with A-site sub-stoichiometry - proved to require significant optimisation of synthetic routes, as described in the experimental section. Here, the phase purity of these routes, according to XRD, is discussed.

Solid state synthesis

XRD patterns of stoichiometric STF powders and two sub-stoichiometric STF powders prepared *via* solid-state synthesis are shown in fig. 4.5. All samples exhibit a cubic perovskite-type phase. However, only the stoichiometric sample appears to be phase pure. Both sub-stoichiometric samples show varying degrees of a secondary phase that was identified as $SrFe_{12}O_{19}$ by comparison with a database. Estimations *via* Rietveld analysis yielded amounts of 0.3 % to 10 % of the secondary phase. Noteworthy, quantification of minor impurity phases is rather inaccurate in XRD. In addition, an XRD pattern of the 3 % sub-stoichiometric target for the PLD is presented in fig. 4.6. Here, no secondary phase is visible, indicating, that the pressing step might assist the solid state reaction, due to more inter-granular contact area.

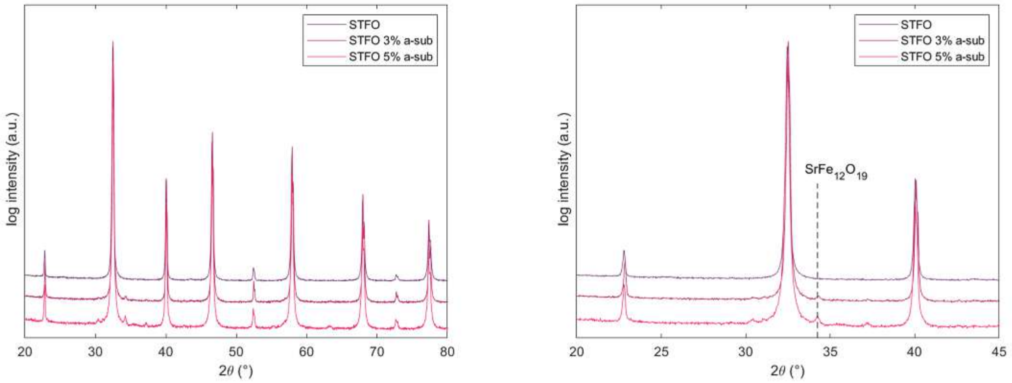

FIGURE 4.5: XRD patterns of stoichiometric und various sub-stoichiometric STF powders prepared *via* solid state synthesis. The most dominant peak of the $SrFe_{12}O_{19}$ phase is marked.

Modified Pechini synthesis

The modified pechini synthesis was performed as described in section 3.2.1. XRD patterns of stoichiometric STF powder and various sub-stoichiometric STF powders prepared *via* the modified Pechini synthesis are shown in fig. 4.7. As above, all samples exhibit a cubic perovskite-type phase. Here, however, the stoichiometric sample as well as the 3 % sub-stoichiometric sample appear phase pure, while secondary phases are visible for the higher A-site deficient samples.

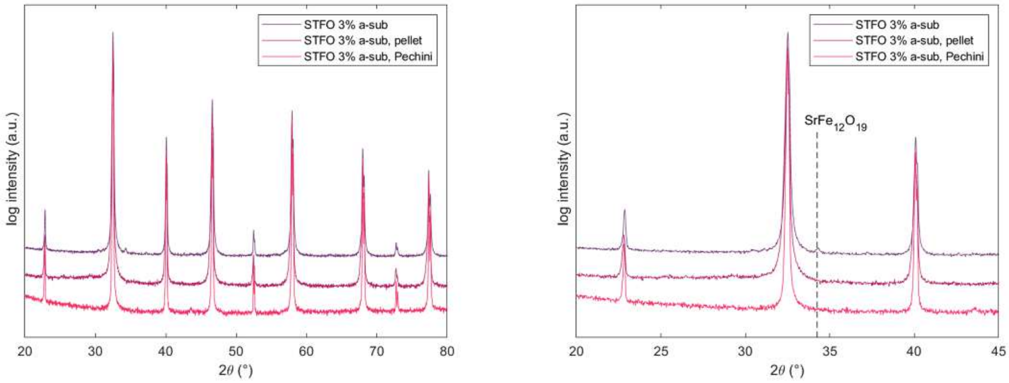

FIGURE 4.6: XRD patterns of 3 % sub-stoichiometric STF powders prepared *via* different routes. The most dominant peak of the SrFe$_{12}$O$_{19}$ phase is marked.

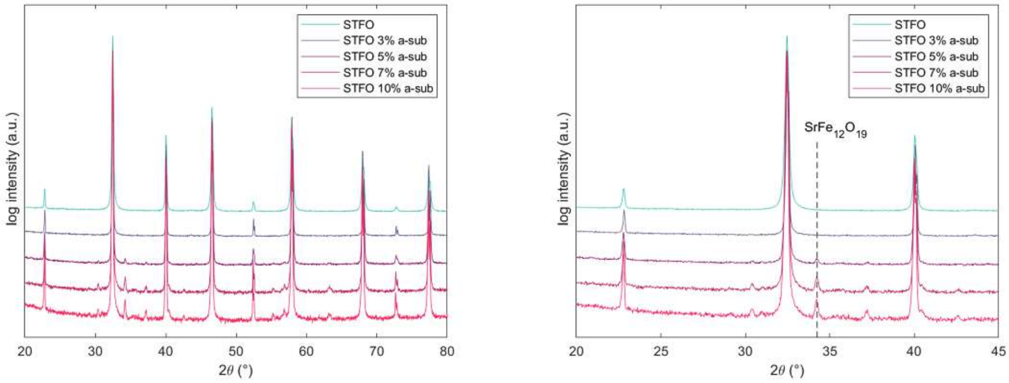

FIGURE 4.7: XRD patterns of stoichiometric STF prepared *via* solid state synthesis und various sub-stoichiometric STF powders prepared *via* Pechini synthesis. The most dominant peak of the SrFe$_{12}$O$_{19}$ phase is marked.

4.2.3 Coulometry

Changes of oxygen stoichiometry vs pO$_2$ of stoichiometric as well as 3 %, 5 % and 7 % sub-stoichiometric STF powders were measured by coulumetry, as described in section 3.5.1. 10 - 30 mg of powder were weighed in each titration cell, and coulometry was performed in intermittent galvanostatic mode at 625 °C, with 0.003 - 0.06 C per galvanostatic step, corresponding to roughly 10^{-3} O atoms per formula unit and step. An exemplary plot of the resulting raw data is presented in fig. 4.2. Measurements were evaluated as described in section 3.7.1. Resulting oxygen stoichiometry vs pO$_2$ curves of STF powders synthesized *via* solid state synthesis are presented in fig. 4.8. As for the LSF samples, a broad stoichiometry plateau is visible at intermediate pO_2. In contrast to the LSF samples, however, the oxygen content does not converge towards a constant value at high pO_2 For all samples, data above an oxygen partial pressure of 10^{-24} bar is in agreement with the defect chemistry model described in section 2.4. Starting at high oxygen partial pressures, the initial decrease in oxygen stoichiometry can be interpreted as the formation of oxygen vacancies, coupled with the filling of electron holes in accordance with eq. ((2.1)). At an oxygen partial pressure between 10^{-7} and 10^{-23} bar, the A-site stoichiometric sample is stable as $Sr_{1-x}Ti_{0.6}Fe_{0.4}O_{2.8}$, with Fe^{3+}, and O^{2-} leading to a plateau of constant stoichiometry. This stoichiometry plateau was chosen as the reference point for the change in oxygen stoichiometry with $\delta = 0$. At lower oxygen partial pressures, the transition from Fe^{3+} to Fe^{2+} starts, leading to a further creation of oxygen vacancies in accordance to eq. ((2.17)).

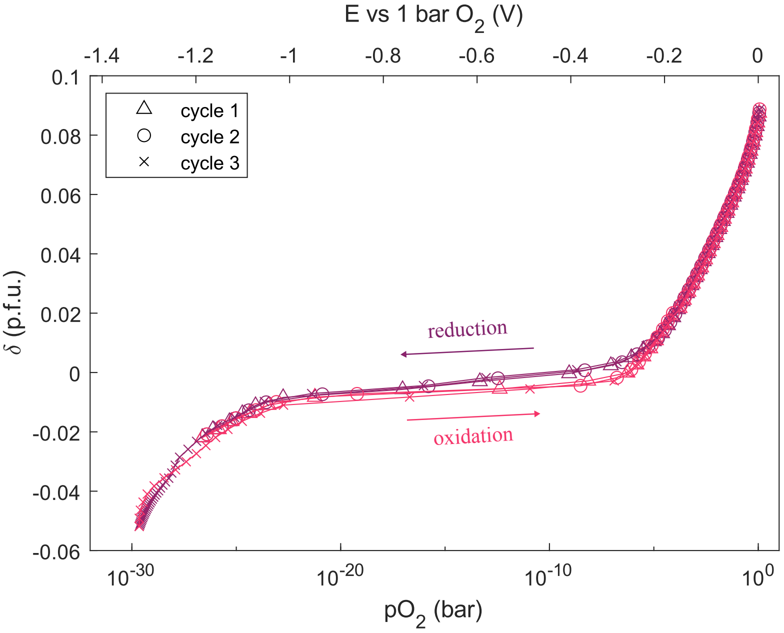

(a) $SrTi_{0.6}Fe_{0.4}O_{2.8-\delta}$

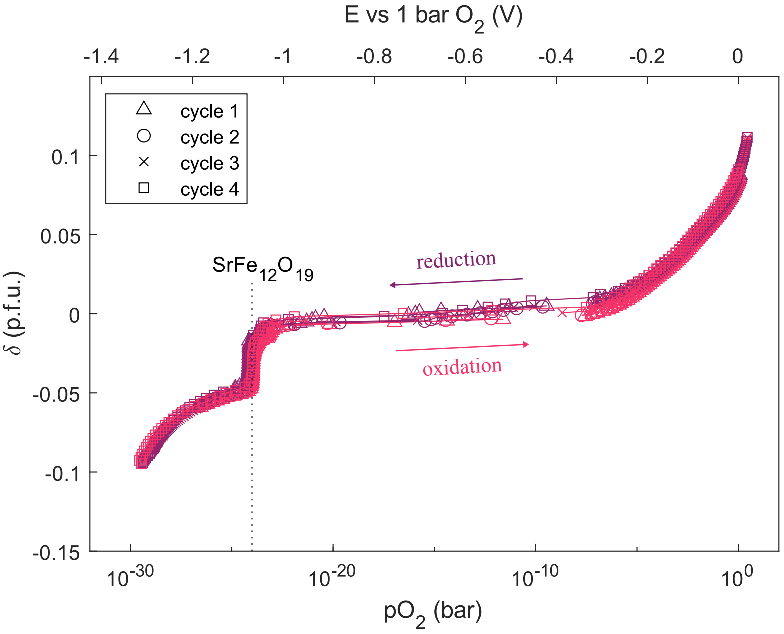

(b) $Sr_{0.97}Ti_{0.6}Fe_{0.4}O_{2.8-\delta}$, calculated amount of Fe in secondary phase: 2.2 %

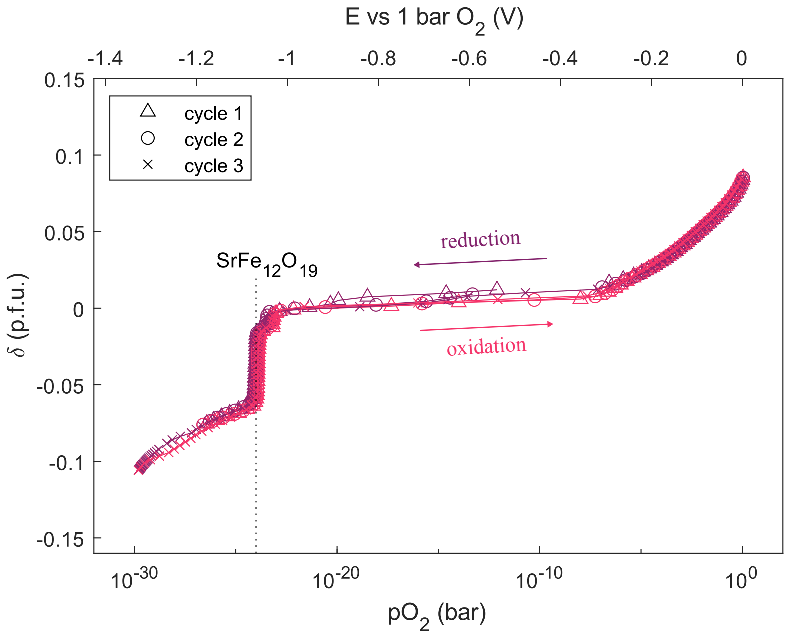

(c) Sr$_{0.95}$Ti$_{0.6}$Fe$_{0.4}$O$_{2.8-\delta}$, calculated amount of Fe in secondary phase: 3.6 %

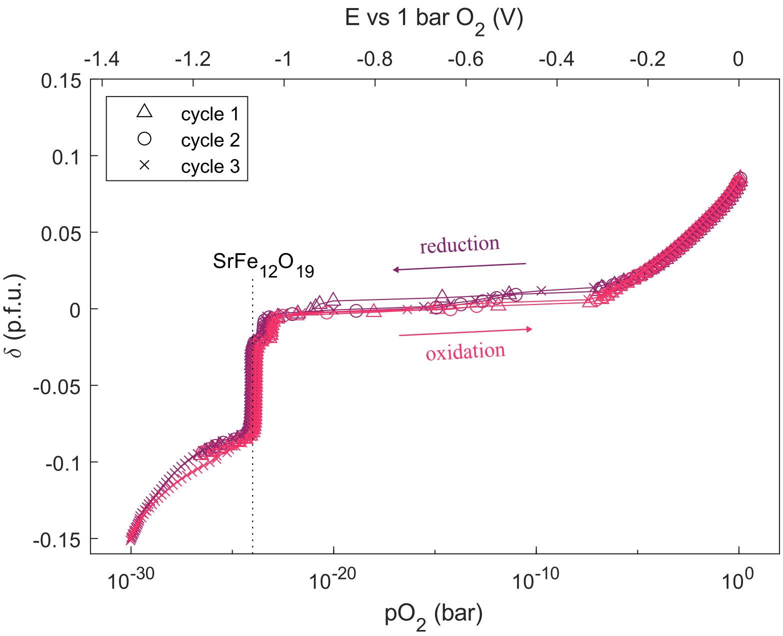

(d) Sr$_{0.93}$Ti$_{0.6}$Fe$_{0.4}$O$_{2.8-\delta}$, calculated amount of Fe in secondary phase: 4.7 %

Figure 4.8: Coulometry curves at 625 °C of SrTi$_{0.6}$Fe$_{0.4}$O$_{2.8-\delta}$ with varying nominal sub-stoichiometry synthesised *via* solid state reaction. The phase transition of the secondary phase is marked.

For the stoichiometric sample, a continuous decrease of oxygen stoichiometry is observable upon further reduction. No phase transition is detectable down to a pO_2 of 10^{-30} bar. The absence of a phase change supports the XRD measurements, which only show a single phase for the stoichiometric sample. In addition, the absence of a phase change indicates that the Fe in the sample is very stable towards reduction to Fe^0. This is supported by the XPS measurements presented in section 4.3.3 as well as the electrochemical analysis of thin film samples (section 4.3.2), which both showed that potentials corresponding to an oxygen activity below 10^{-30} bar were necessary for the exsolution of metallic iron.

For the sub-stoichiometric samples synthesised *via* solid state reaction, a phase transition is observable at a pO_2 of 10^{-24} bar. In accordance with the XRD measurements, this phase transition is assumed to stem from $SrFe_{12}O_{19}$. The percentage of secondary phase was quantified according to section 3.7. Calculated percentages of secondary phases are presented in table 4.3. As can be seen, the amount of secondary phase shows good correlation with the nominal sub-stoichiometry for the samples synthesised *via* solid-state synthesis. This suggests, that the effective sub-stoichiometry of those samples is in fact a lot smaller and the excess B-site ions get compensate *via* the formation of the Fe-rich $SrFe_{12}O_{19}$ phase.

TABLE 4.3: Calculated amount of Fe in secondary phases for STF powder samples $\left(\frac{n_{(\text{Fe in secondary phase})}}{n_{(\text{STF})}}\right)$.

Sample	amount of Fe secondary phase (%)
STF97P	0.4
STF97	2.2
STF95	3.6
STF93	4.7

The oxygen stoichiometry vs pO_2 curve for the 3 % sub-stoichiometric sample synthesised *via* the modified Pechini route is shown in fig. 4.9. Here, a phase transition at a pO_2 of 10^{-24} bar is visible as well, albeit smaller than for 3 % sub-stoichiometric the sample synthesized *via* the solid state reaction. This suggest, that the sample synthesised *via* the modified Pechini route consists of a smaller amount of $SrFe_{12}O_{19}$ as well as a sub-stoichiometric STF with a sub-stoichiometry < 3 %. As there was no secondary phase observed in the XRD, it is assumed that the amount of secondary phase present is below the detection limit of the XRD. Upon further reduction a continuous decrease in oxygen stoichiometry down to a pO_2 of 10^{-32} bar without any further phase transition is observable. This corresponds to the continuous formation of oxygen vacancies, coupled with the formation of Fe^{2+}. Also, the good reproducibility of the

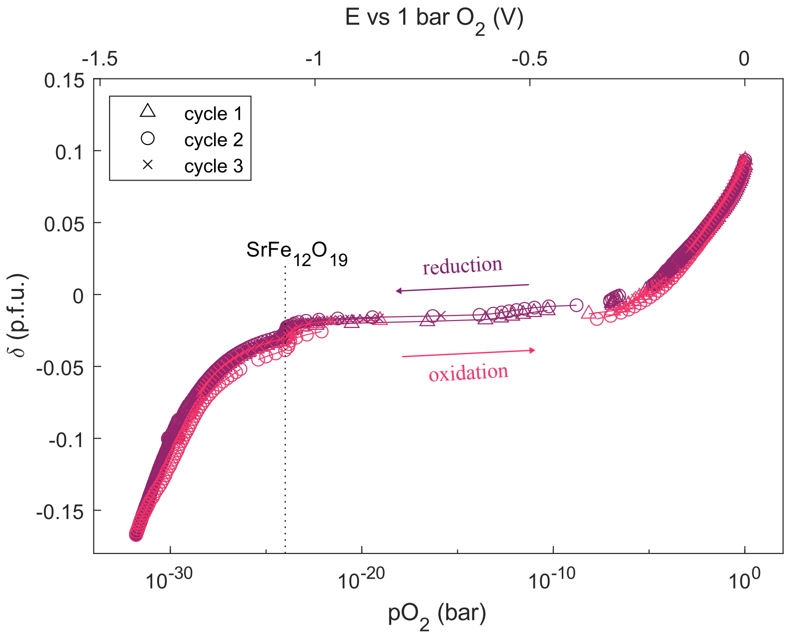

FIGURE 4.9: Coulometry curve of $Sr_{0.97}Ti_{0.6}Fe_{0.4}O_{2.8-\delta}$ prepared *via* the Pechini method. The phase transition of a secondary phase is visible, although smaller than for the 3 % sub-stoichiometric sample synthesised by solid state synthesis. Calculated amount of Fe in secondary phase: 0.4 %.

subsequent cycles indicates that no irreversible Fe metal exsolution took place. Noteworthy, such highly reducing gas phase conditions correspond to a $H_2 : H_2O$ mixing ratio of 30000 : 1 - which is not easy to achieve in a typical thermo-gravimetry apparatus. The high reduction stability of STF is also supported by the XPS measurements presented in section 4.3.3.

4.3 $SrTi_{0.6}Fe_{0.4}O_{2.8-\delta}$ thin films

4.3.1 Scanning electron microscopy

Uncapped thin films

For the investigation of the oxygen exchange kinetics, STF films were deposited on (100) oriented YSZ single crystals with a Pt thin film current collector grid, and a porous GDC-based counter electrode, as described in detail in section 3.2.3. SEM images of all uncapped thin film

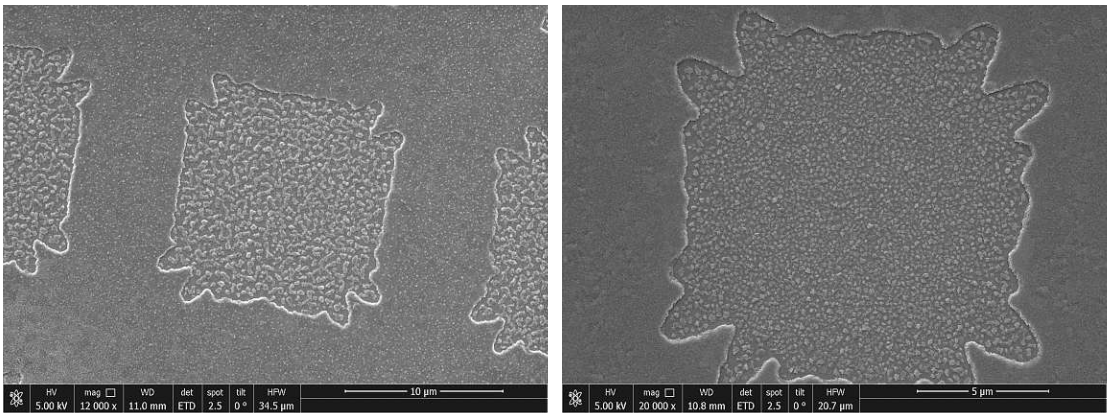

(a) $SrTi_{0.6}Fe_{0.4}O_{2.8-\delta}$ **(b)** $Sr_{0.97}Ti_{0.6}Fe_{0.4}O_{2.8-\delta}$

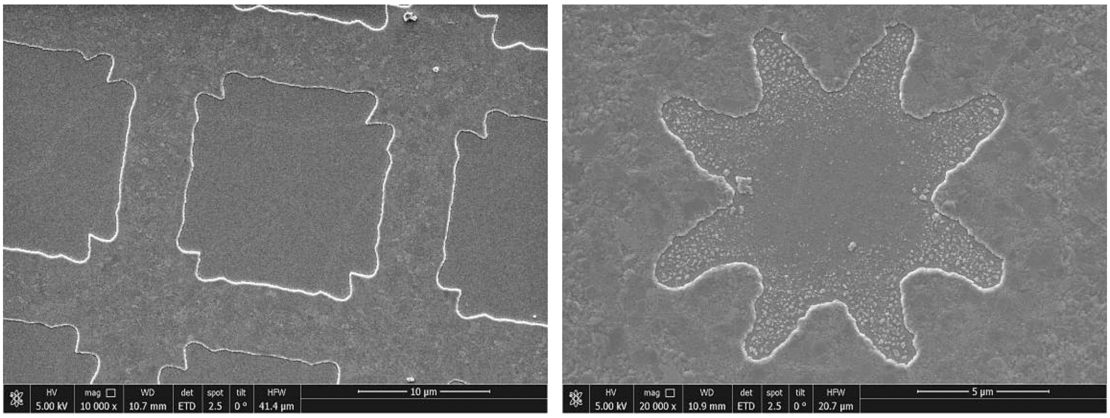

(c) $Sr_{0.95}Ti_{0.6}Fe_{0.4}O_{2.8-\delta}$ **(d)** $Sr_{0.93}Ti_{0.6}Fe_{0.4}O_{2.8-\delta}$

FIGURE 4.10: SEM images of the uncapped STF thin films with varying sub-stoichiometry. For all samples apart from the 5 % sub-stoichiometric STF, the current collector grids appear non-ideal.

samples are presented in fig. 4.10. The lithography mask consisted of a square grid with 5 μm wide stripes and holes of 15x15 μm^2. However, due to diffraction artifacts during the UV illumination step, the final current collector is not well defined and covers more than the nominal 43.75% of the single crystal. In addition, the ion etching process appears to be incomplete for some samples, leading to a poorly defined thin film structure and less contact area between STF thin film and the single crystal electrolyte. This non-ideal current collector might be the reason for some difficult to interpret electrochemical behaviour observed in section 3.7.2.

Capped thin films

Capped thin films were prepared similarly to the uncapped films, but on these the oxygen exchange reaction was largely blocked by a thick zirconia top layer, in order to get more information on the oxygen stoichiometry changes of the sample. SEM images of capped thin films are presented in figs. 4.11 to 4.13 . As for the uncapped samples, the current collector appears to be non-ideal, potentially leading to the electrochemical feature observed in section 3.7.2. Cross sections of the capped sample reveal a fairly homogeneous film thickness of about 330 nm across all samples, which is in line with the film thickness measurements performed with the quartz microbalance.

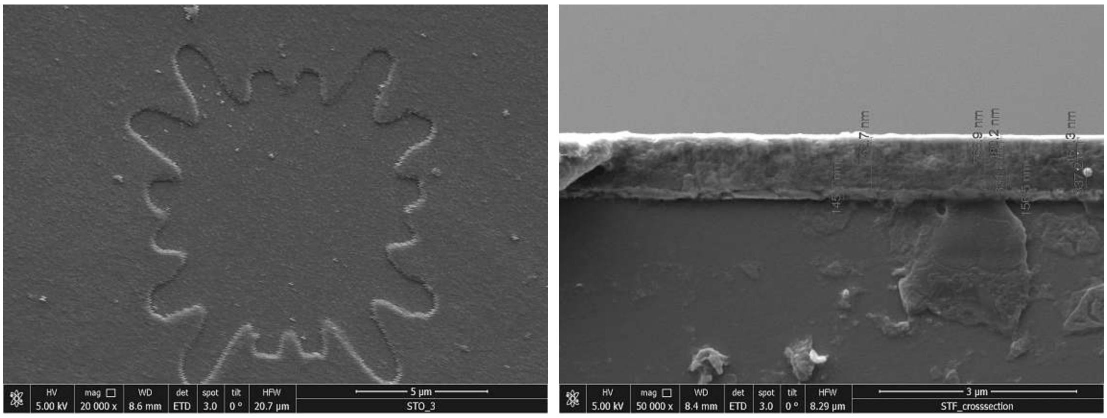

(a) Top view showcasing the irregular current collector grid.

(b) Cross-section showcasing the current collector, ~330 nm STF layer and ZrO_2 capping layer.

FIGURE 4.11: SEM image of capped stoichiometric STF thin film.

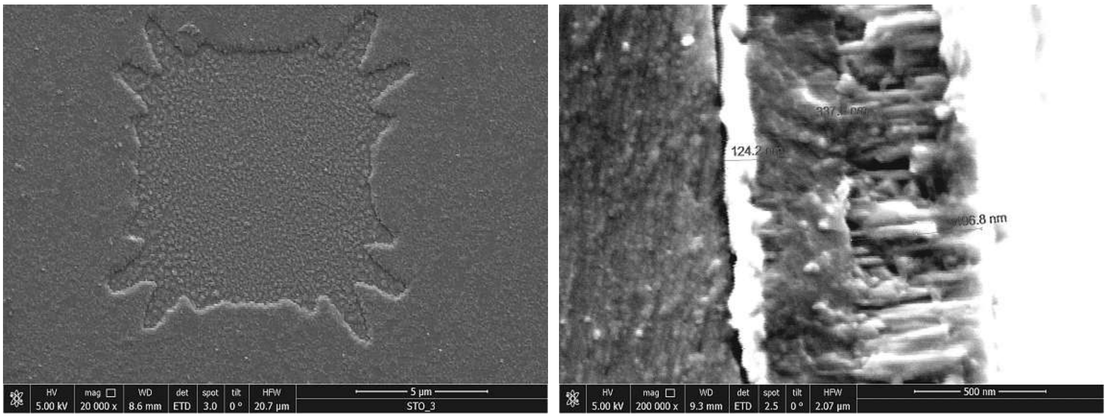

(a) Top view showcasing the irregular current collector grid. **(b)** Cross-section showcasing the current collector, ~330 nm STF layer and ZrO_2 capping layer.

Figure 4.12: SEM image of capped 3 % A-sub STF thin film.

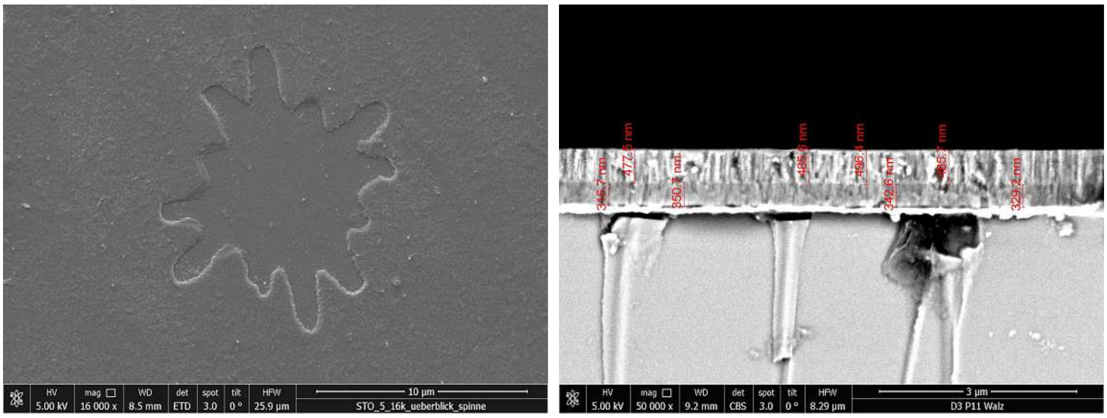

(a) Top view showcasing the irregular current collector grid. **(b)** Cross-section showcasing the current collector, ~330 nm STF layer and ZrO_2 capping layer.

Figure 4.13: SEM image of capped 5 % A-sub STF thin film.

4.3.2 Electrochemical analysis of capped thin films

On the capped STF films, impedance spectra and potentiostatic coulometry with 20 mV voltage step resolution were acquired at 480 °C and 625 °C in N_2 atmosphere containing about ~10 ppm of O_2. The oxygen partial pressure was monitored by using the Fe+FeO-filled titration cell as a single-atmosphere Lambda probe (see section 3.5.2) with an internal reference pO_2 of 10^{-24} bar. An exemplary plot of the resulting raw data for the coulometry is presented in fig. 4.14. The current peaks at the start and end of each EIS spectrum are caused by voltage fluctuations due to the EIS measurements and were excluded from the evaluation. Oxygen stoichiometry changes of the thin films were calculated from the chemical capacitance derived from the EIS spectra as well as the current relaxation feature in the coulometry measurements, as described in detail in section 3.7.2.

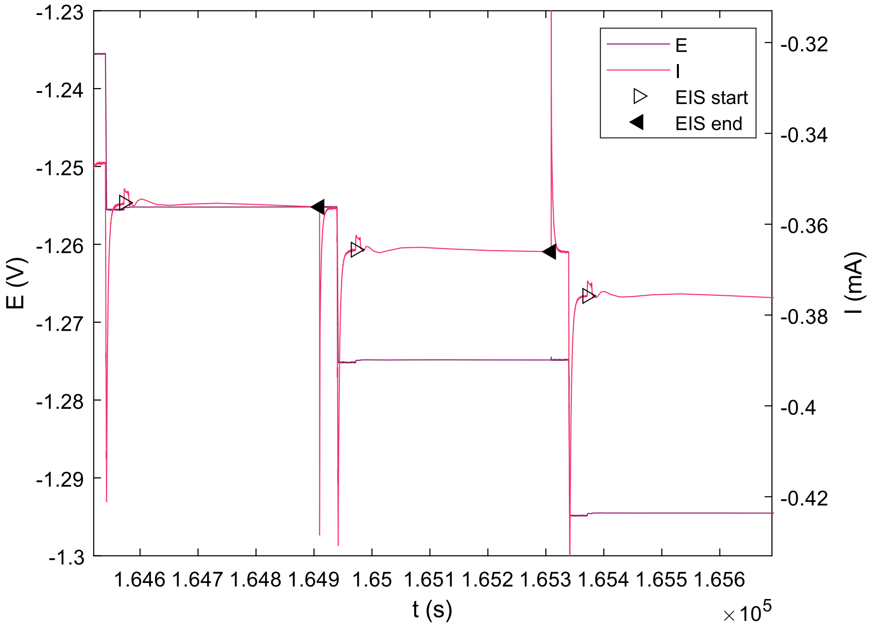

FIGURE 4.14: Exemplary raw data for the coulometry of thin film samples. Current peaks at the beginning and at the end of the EIS measurements are artefact caused by voltage fluctuations. Shown is the stoichiometric sample at 625 °C.

$SrTi_{0.6}Fe_{0.4}O_{2.8-\delta}$

The $a(O_2)$ dependence of the oxygen stoichiometry of the stoichiometric sample at 480 °C is plotted in fig. 4.15a. Data points were calculated from the EIS measurements as described in section 3.7.2. For thin film samples, δ vs $a(O_2)$ curves calculated from the coulometry measurements are not included, as the leakage current leads to artifacts that complicate the interpretation. An example is presented in fig. 4.17.

Within a wide $a(O_2)$ range the reaction remains perfectly reversible, showing the same general behavior as the stoichiometric powder sample (section 4.2.3). Starting at high $a(O_2)$, a decrease of the $a(O_2)$ leads to the formation of oxygen vacancies, coupled with the filling of electron holes in accordance with eq. ((2.1)). This is followed by a stoichiometry plateau at a a(O_2) range of 10^{-6} to 10^{-33} bar. Further decreasing the a(O_2) again leads to the formation of oxygen vacancies, coupled to the transition of Fe^{3+} to Fe^{2+}. Within the whole a(O_2) range, no phase transition is observable. The corresponding chemical capacitance vs a(O_2) curve is shown in fig. 4.15b. Data points were calculated from EIS measurements and coulometry as described in section 3.7.2. In contrast to the δ vs a(O_2) curves, the error caused by the leakage current is not cumulative in the C_{chem} vs a(O_2) curves. Thus, the data points obtained from the coulometry measurements can be used here.

Starting at high a(O_2), the high initial chemical capacitance can be explained with the equilibrium between electron holes and oxygen vacancies (eq. ((2.1))). Shifting this equilibrium to the oxygen vacancy side by decreasing the pO_2 decreases the chemical capacitance until a minimum is reached at the middle of the stoichiometry plateau. Further decreasing the a(O_2) leads to a transition of Fe^{3+} to Fe^{2+} coupled to the creation of new oxygen vacancies. This in turn leads to an increase of chemical capacitance with a maximum roughly at a(Fe^{3+}) = a(Fe^{2+}). Apart from a regime at low a(O_2), EIS and coulometry data are in good agreement. Below 10^{-35} bar, the chemical capacitance derived from EIS is substantially higher. Here, we deem the values derived from EIS more reliable. Firstly, the current in the coulometry measurements reaches the equilibrium slower at low a(O_2). When the constant voltage step ends before equilibrium is reached, the reactive "leakage" current is slightly over-estimated. Moreover, this leakage current increases significantly at low p(O_2), so the determination of the current spike in the coulometry is more prone to errors. Consequently, we focus our further discussion on the non-stoichiometry derived from the EIS measurements. In summary, the thermo-chemical stability of stoichiometric STF films appears to be very high, and higher temperatures are required to test the stability limit.

The a(O_2) dependence of the oxygen stoichiometry and chemical capacitance of the stoichiometric sample at 625 °C is shown in fig. 4.16. The same general trend as for the measurement performed at 480 °C is observable. However, an irreversible reaction occurs during the first reduction, which can clearly be noticed in the chemical capacitance vs a(O_2) curve. For the first reduction, the chemical capacitance at intermediate a(O_2) (10^{-16} bar) is lower than for all consecutive runs. In addition, the chemical capacitance maximum at low a(O_2) (10^{-33} bar) is higher during the first reduction than for all consecutive runs. These phenomena could be explained by the formation of Fe^0 particles. During the first reduction, an exsolution of Fe^0 at low a(O_2) leads to an increase of chemical capacitance there. Subsequent re-oxidation of the sample also leads to the re-oxidation of Fe. The re-oxidation of Fe, however, is marked by an (at least partial) formation of Fe_2O_3 which leads to a higher chemical capacitance at intermediate a(O_2). It is noteworthy, that reducing the a(O_2) below the chemical capacitance maximum at 10^{-33} bar

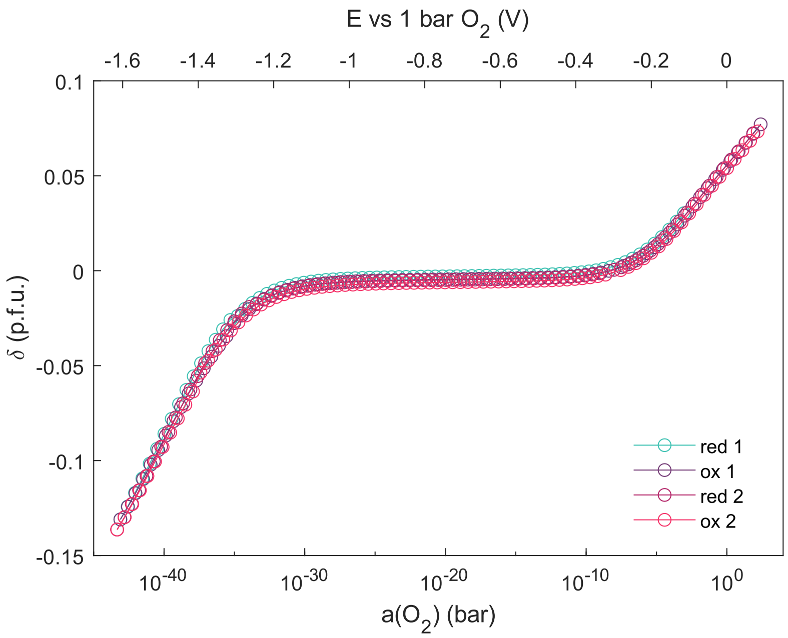

(a) Change in oxygen stoichiometry vs a(O_2) (EIS only).

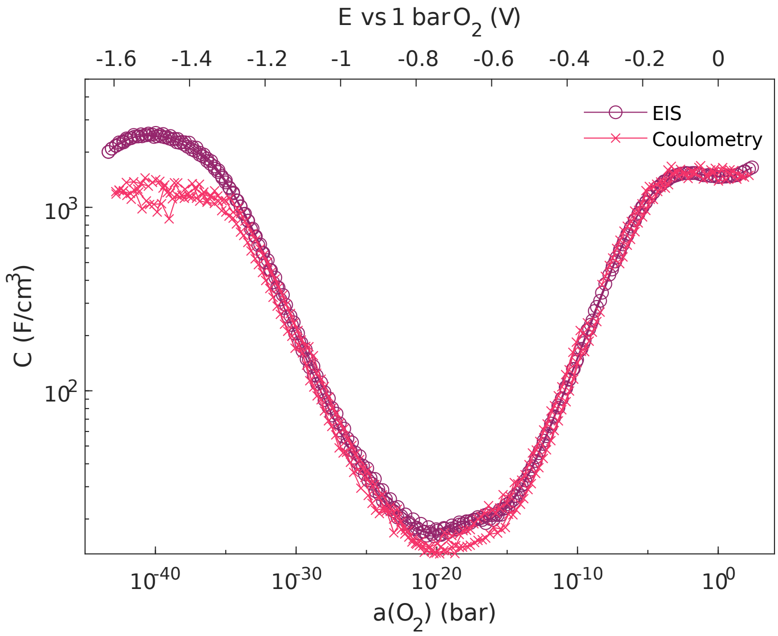

(b) Capacitance vs a(O_2).

FIGURE 4.15: Electrochemical data of the capped $SrTi_{0.6}Fe_{0.4}O_{3-\delta}$ at 480 °C.

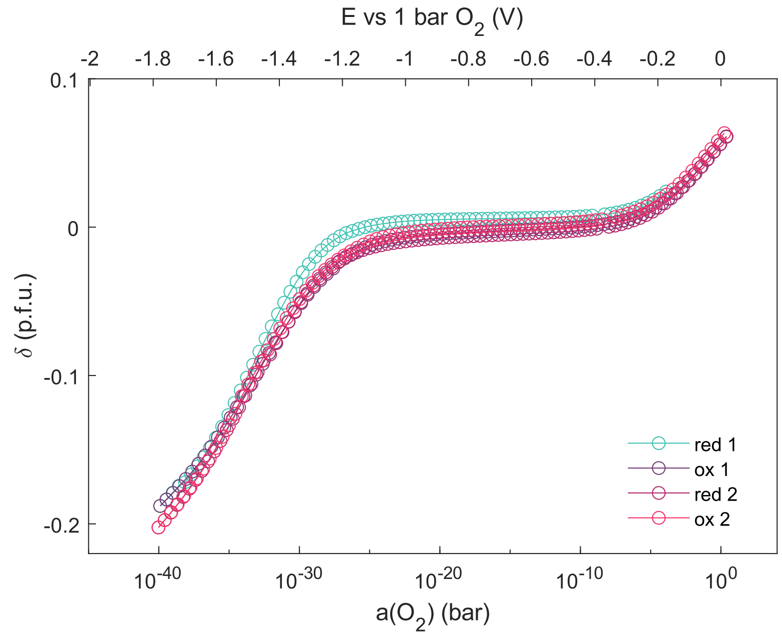

(a) Change in oxygen stoichiometry vs $a(O_2)$ (EIS only).

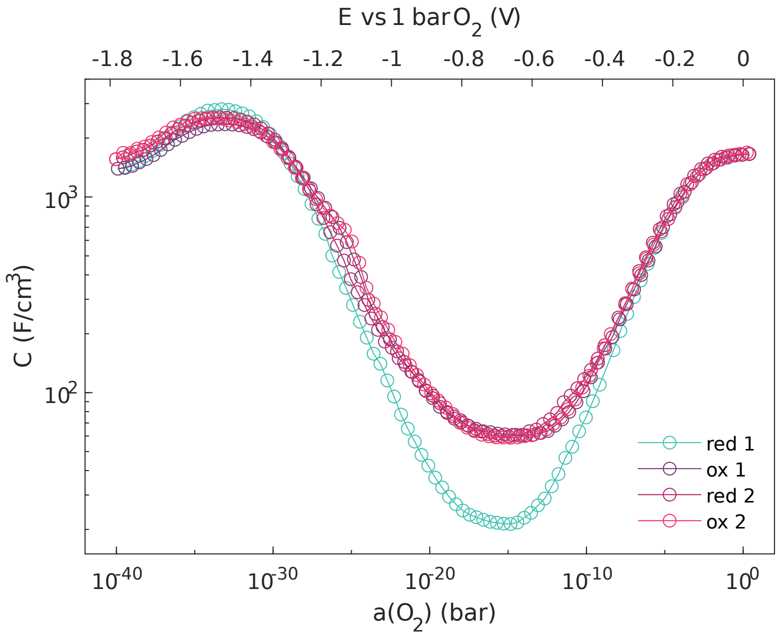

(b) Capacitance vs $a(O_2)$ (EIS only).

FIGURE 4.16: Electrochemical data of the capped $SrTi_{0.6}Fe_{0.4}O_{2.8-\delta}$ at 625 °C.

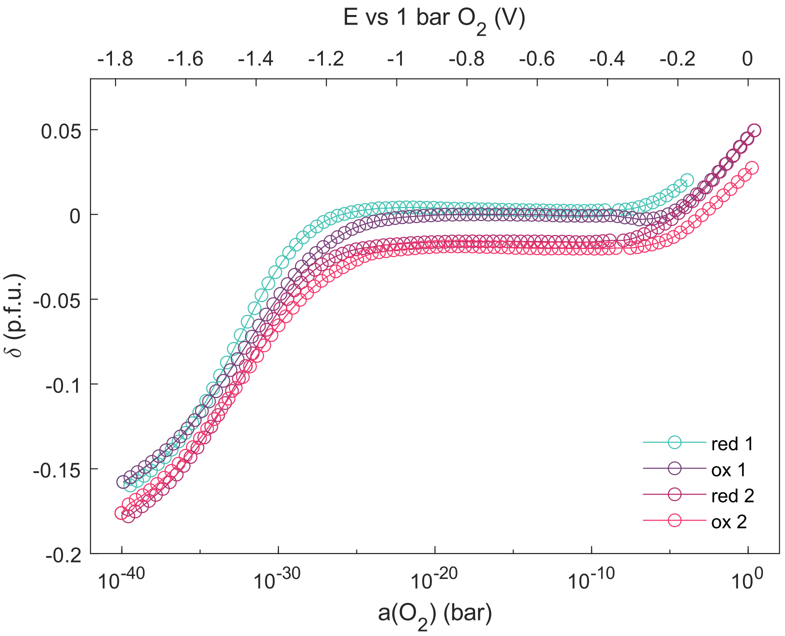

Figure 4.17: Exemplary oxygen stoichiometry vs a(O_2) curve derived from coulometry measurements, showing the cumulative effect of the leakage current, which complicates the interpretation of the data. Presented is the stoichiometric sample at 625 °C.

does not lead to a fast decrease in chemical capacitance, which would be expected when the capacitance maximum stems from the reduction of Fe^{3+} to Fe^{2+} only. In this case, one would also expect a second stoichiometry plateau at $\delta = -0.2$. The absence of this secondary plateau can be explained with the XPS measurements (section 4.3.3), which showed that the a(O_2) regime at which the transition from Fe^{3+} to Fe^{2+} occurs overlaps with the a(O_2) regime at which the transition from Ti^{4+} to Ti^{3+} occurs. The high chemical capacitance below the maximum at a a(O_2) of 10^{-33} bar can thus be described by a combined contribution of transition from Fe^{3+} to Fe^{2+} and Ti^{4+} to Ti^{3+}. In summary, very reducing conditions are required to trigger irreversible processes in stoichiometric STF at 625°C, which can only be achieved by direct electrochemical reduction, while even dry H_2 atmosphere (with some ppm of H_2O) is not sufficiently reducing.

$Sr_{0.97}Ti_{0.6}Fe_{0.4}O_{2.8-\delta}$

Oxygen stoichiometry and chemical capacitance vs a(O_2) curves of 3 % sub-stoichiometric STF down to 10^{-27} bar are presented in fig. 4.18. Data points were calculated as described in section 3.7.2. The thin film sample behaves in a similar way to the powder counterpart, exhibiting a stoichiometry plateau at a a(O_2) between 10^{-7} and 10^{-23} bar. In contrast to the powder samples, no phase transition is observable down to an oxygen partial pressure of 10^{-27} bar. As for the stoichiometric STF thin film, the chemical capacitance exhibits a maximum at high a(O_2), then decreases with decreasing a(O_2) until it reaches a minimum at 10^{-16} bar a(O_2) and increase again with a further decrease of a(O_2). Data points of the coulometry and EIS are in good agreement, albeit the coulometry becomes noisy at low chemical capacitance. This is due to the leak current getting bigger in relation to the transient current spike associated with the chemical capacitance at lower chemical capacitance. Within the given a(O_2) range the reaction remains fully reversible.

Oxygen stoichiometry and chemical capacitance vs a(O_2) curves of 3 % sub-stoichiometric STF down to 10^{-35} bar are presented in fig. 4.19. Here, an irreversible reaction is present that, as for the stoichiometric STF thin film, is observable as a deviation of the EIS data points for the first reduction from all consecutive runs. Comparing the EIS data with the data from the simultaneously performed coulometry reveals a peak at 10^{-24} bar a(O_2) during the oxidation steps, which remains mostly hidden in the EIS data. This is the a(O_2), which was found to correlate to the oxidation of Fe metal, see fig. 4.4. This supports the hypothesis that the change in chemical capacitance is caused by the irreversible exsolution of Fe, which does not get re-incorporated into the perovskite upon re-oxidation but instead forms a Fe_2O_3 phase.

$Sr_{0.95}Ti_{0.6}Fe_{0.4}O_{2.8-\delta}$

Oxygen stoichiometry and chemical capacitance vs a(O_2) curves of 5 % sub-stoichiometric STF down to 10^{-35} bar are presented in fig. 4.20. General trends for both curves are in line with the interpretations given in section 4.3.2. As for the 3 % sub-stoichiometric sample, the presence of an irreversible reaction can not only be observed as a change in the EIS data points, but also as an (less pronounced) peak in the data points obtained from the coulometry at a a(O_2) of 10^{-24} bar.

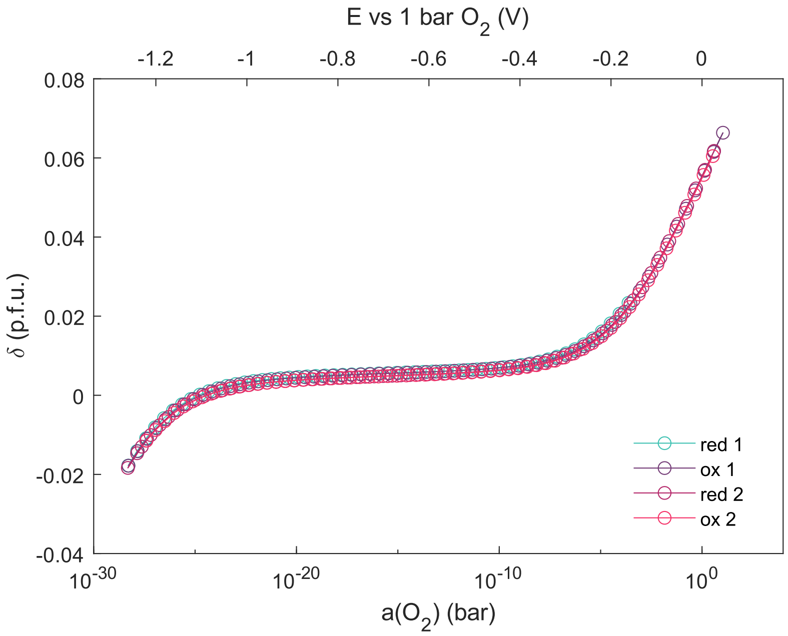

(a) Change in oxygen stoichiometry vs a(O_2) (EIS only).

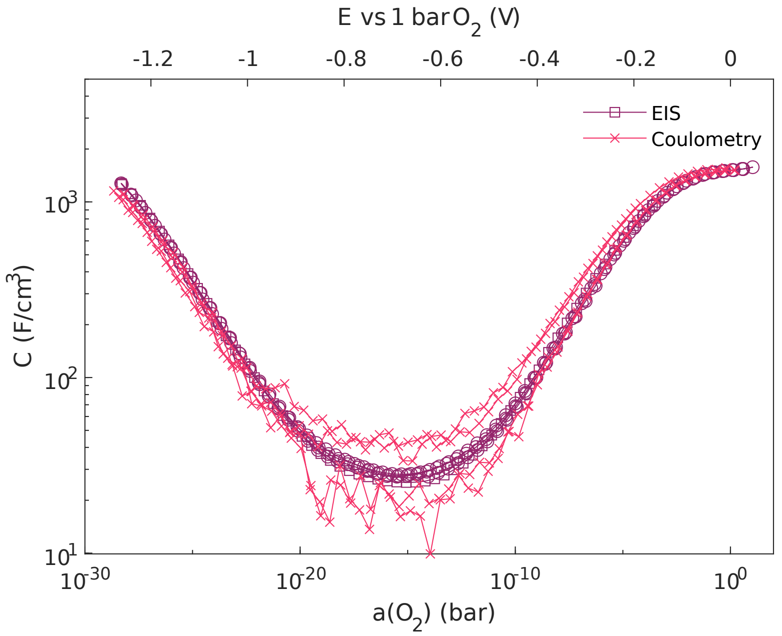

(b) Capacitance vs a(O_2).

Figure 4.18: Electrochemical data of the capped $Sr_{0.97}Ti_{0.6}Fe_{0.4}O_{2.8-\delta}$ at 625 °C with a fully reversible reaction.

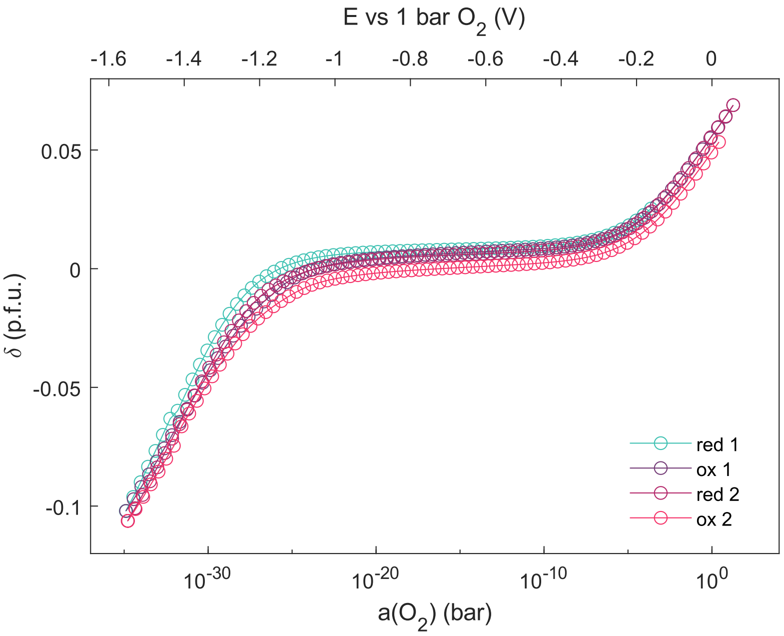

(a) Change in oxygen stoichiometry vs a(O_2) (EIS only).

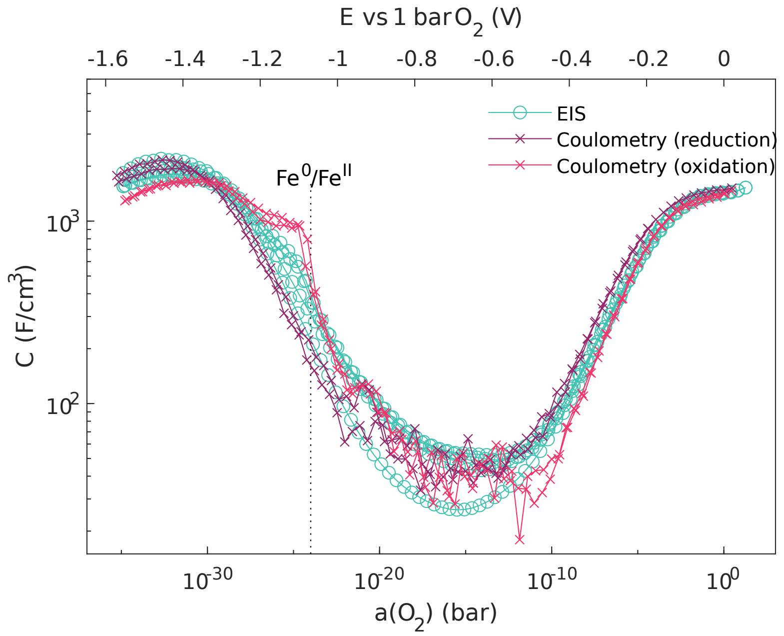

(b) Capacitance vs a(O_2), the transition of Fe^0 to Fe^{2+} is marked.

FIGURE 4.19: Electrochemical data of the capped $Sr_{0.97}Ti_{0.6}Fe_{0.4}O_{2.8-\delta}$ at 625 °C with an irreversible reaction during the first reduction.

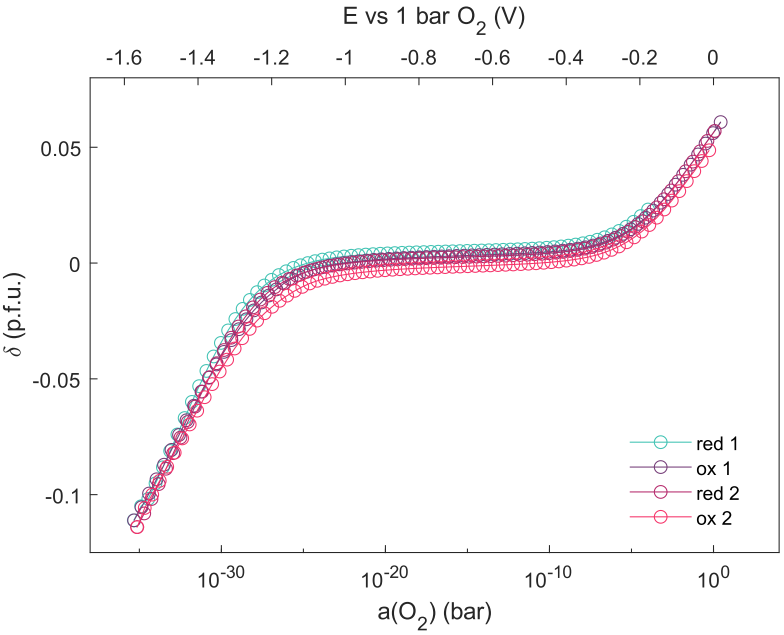

(a) Change in oxygen stoichiometry vs $a(O_2)$ (EIS only).

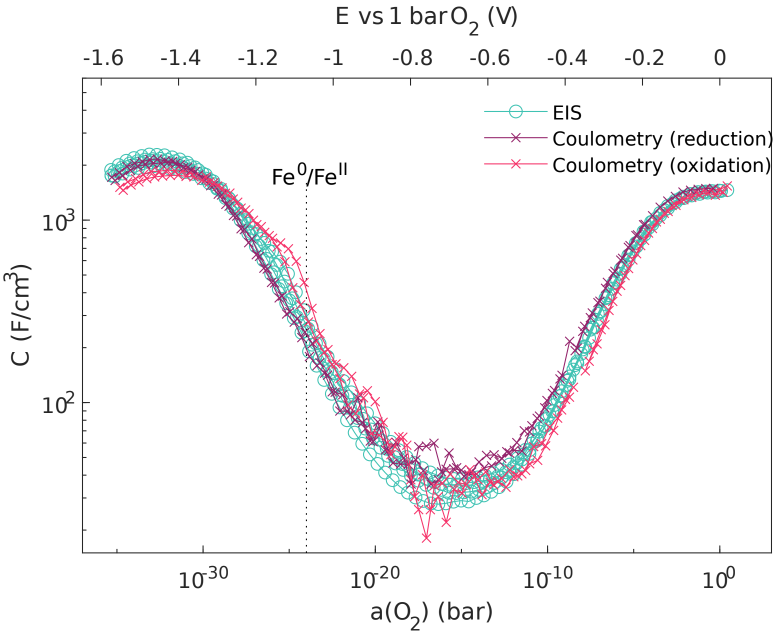

(b) Capacitance vs $a(O_2)$, the transition of Fe^0 to Fe^{2+} is marked.

Figure 4.20: Electrochemical data of the capped $Sr_{0.95}Ti_{0.6}Fe_{0.4}O_{2.8-\delta}$ at 625 °C.

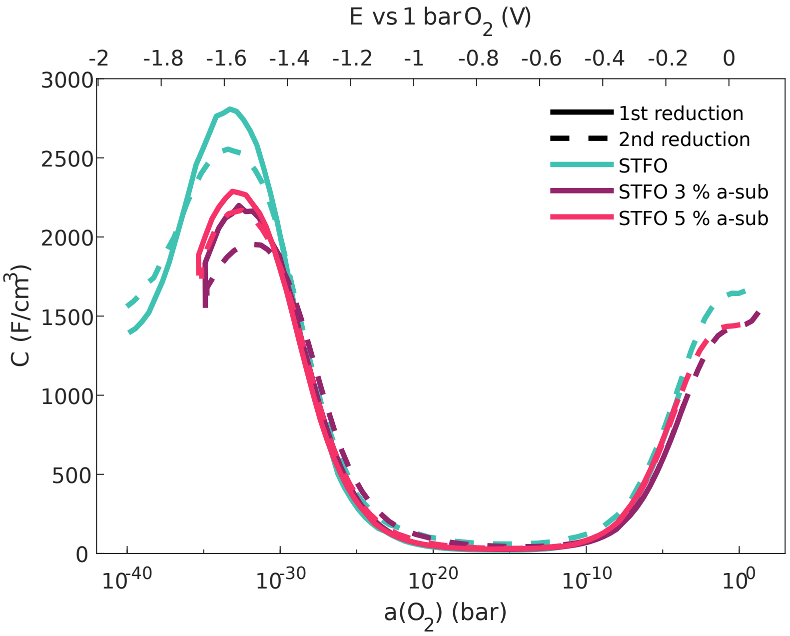

Figure 4.21: Comparison of the capacitance (linearly plotted) of STF thin films with varying sub-stoichiometry. Only data obtained from EIS measurements and reductive half cycles are shown.

Comparison

Comparing a(O_2) curves of all three capped thin film samples (fig. 4.21), a decrease of the chemical capacitance peak at low a(O_2) with increasing sub-stoichiometry is noticeable. This might be explained with the presence of antisite defects in the sub-stoichiometric samples (section 2.1). As the chemical capacitance at low a(O_2) is assumed to stem from the transition of Fe^{3+} to Fe^{2+}, a lower concentration of Fe^{3+} would thus decrease the chemical capacitance at low (O_2).

4.3.3 X-ray photoelectron spectroscopy

XPS was performed on thin-film model cells with a STF95 and STF100 electrode and oxygen buffering counter electrode that relies on the principle of a Fe/FeO phase equilibrium. Voltage variation was performed at 400 °C and subsequently at 625 °C cell temperature. Fe, Ti, Sr and O spectra were acquired at each voltage setpoint. In addition, changes in oxygen stoichiometry were measured *via* EIS for STF95 and *via* coulometry for STF100, as described in section 3.7.2.

An exemplary plot of the raw data from the coulometry is presented in fig. 4.22. Noteworthy, in contrast to the coulometry performed on capped samples, almost no leakage current is detectable due to the negligible gas phase present.

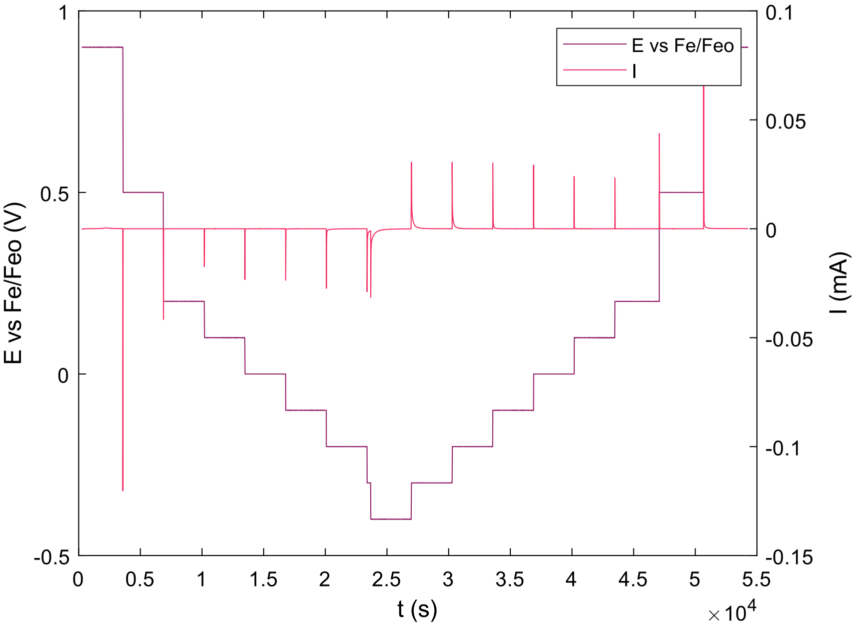

Figure 4.22: Exemplary raw data for the coulometry performed alongside the XPS measurements at 400 °C. Noteworthy, the leakage current converges to zero.

First, it is important to confirm that the oxygen activity is indeed controllable by means of the cell voltage. This requires, that the kinetic overpotentials are negligible due to negligible current (virtually open circuit conditions). For this, we used the sensitivity of XPS measurements toward Fermi level changes. The "binding energy" in XPS is actually not the total binding energy of the electron, but the energy difference between core level energy and Fermi level. As a reduction of a mixed conductor means fewer electron hole and more "electron" or Fe^{2+} defects, the Fermi level moves upwards upon reduction. In the case of acceptor doped perovskites with predominant oxygen vacancy compensation of the dopant charge – as is the case here – the Fermi energy changes with the cell voltage with a slope of -1 eV/V, and so does the measured binding energy of core levels of non redox-active elements. To confirm this, in fig. 4.23 the binding energy of the Ti 2p$_{3/2}$ peak as a function of the cell voltage is presented. As can be seen for both samples and all conditions, the Ti 2p binding energy is an excellent measure for the oxygen activity within the sample.

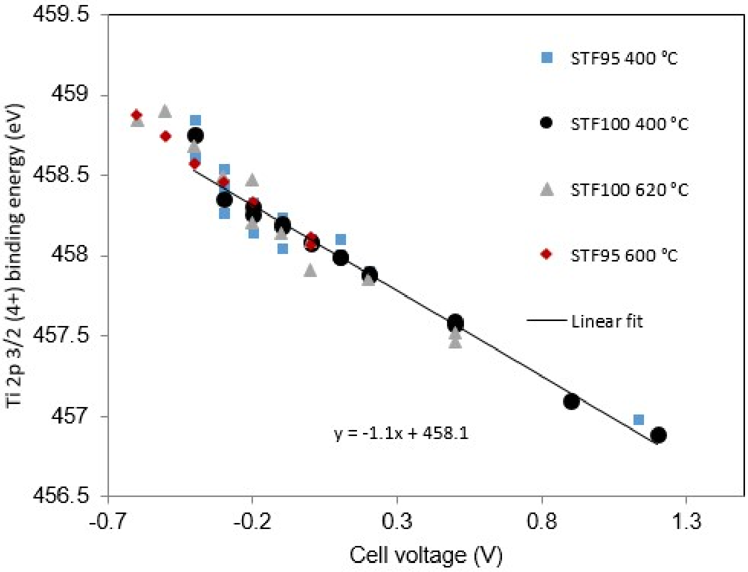

FIGURE 4.23: Measured binding energy of the Ti^{4+} $2p_{3/2}$ component as function of the working electrode voltage vs an Fe/FeO counter and reference electrode for STF100 and STF95 thin films at 400 °C and 600 °C.

The oxidation states of Fe and Ti were fitted by a peak model, see fig. 4.24. In reducing conditions, the Ti 2p peak gets slightly broader and asymmetric, which can be interpreted as an onset of the reduction of Ti^{4+} to Ti^{3+}. Also the Fe 2p peak shape changes in reducing conditions, and a Fe^{2+} as well as metallic Fe species become visible in sufficiently reducing conditions. The Sr 3d spectra appear to be hardly at all influenced by the polarization, apart from the energy shift. The assignment “bulk” and “surface” for the two Sr components is according to previous studies in which depth-profiling was performed [36]. In order to gain a robust fit, the energy separation and Full Width Half Maximum (FWHM) of the peaks of each oxidation state was fixed, and only relative areas were varied. For each Fe oxidation state, multiple components were used and constrained in relative positions, areas and FWHM, in order to get appropriate fingerprint shapes of each oxidation states as suggested in [37, 38].

The fractions of the different observed oxidation states as function of the working electrode oxygen activity are plotted in fig. 4.25 at 400 °C and 625 °C for STF100 and STF95. No Fe metal exsolution was observed by reduction at 400 °C, and the process appeared perfectly reversible. Also Fe in STF95 appears to be slightly more reducible but the difference is minimal. However,

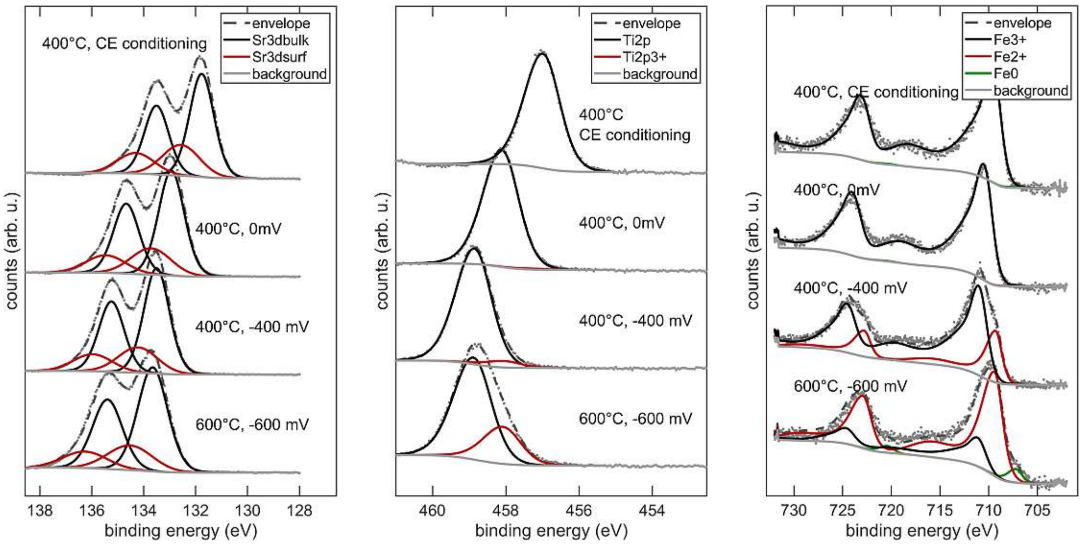

FIGURE 4.24: XPS spectra of the STF95 thin film sample at different conditions. Sr 3d, Ti $3d_{5/2}$ and Fe 2p transitions are shown. Grey dots represent the counts, and solid and dashed lines the fit results.

at a higher temperature of 600 °C, Fe metal exsolution starts at $\sim 10^{-32}$ bar, corresponding to a cell voltage of -300 mV. Also here, slightly more Fe^{0} and Fe^{2+} are found for STF95, but again with minimal effect. In addition, the estimated surface and bulk oxygen stoichiometry is given by the data lines “Delta”. The surface oxygen stoichiometry was calculated from the XPS data, by using the charge neutrality equation in the form of

$$3 - \delta = 2.8 - 0.3[Ti^{3+}] - 0.2[Fe^{2+}] - 0.6[Fe^{0}]. \tag{4.1}$$

Therein $[Ti^{3+}]$, $[Fe^{2+}]$ and $[Fe^{0}]$ are the relative amounts of Ti^{3+}, Fe^{2+} and metallic iron respectively. The values gained thereby (blue curves, named Delta(XPS)) are in good agreement with the thin film coulometry, and rather similar for STF100 and STF95 (with STF95 being slightly more reduced). The electrically measured non-stoichiometry (Delta(DC) and Delta(EIS) for STF100 and STF95 respectively), however, differs massively between the two samples. This lies most likely in the different methods used – for STF100, the changes in oxygen stoichiometry were determined *via* coulometry (which is quite reliable here, since almost no leakage current is present). For STF95, however, EIS measurements were used to determine the changes in oxygen stoichiometry. As discussed earlier, the formation of Fe metal is not well observable by EIS, due to the irreversibility of the process. Consequently, this method delivers a much smaller oxygen sub-stoichiometry leading to the discrepancy between the electrically

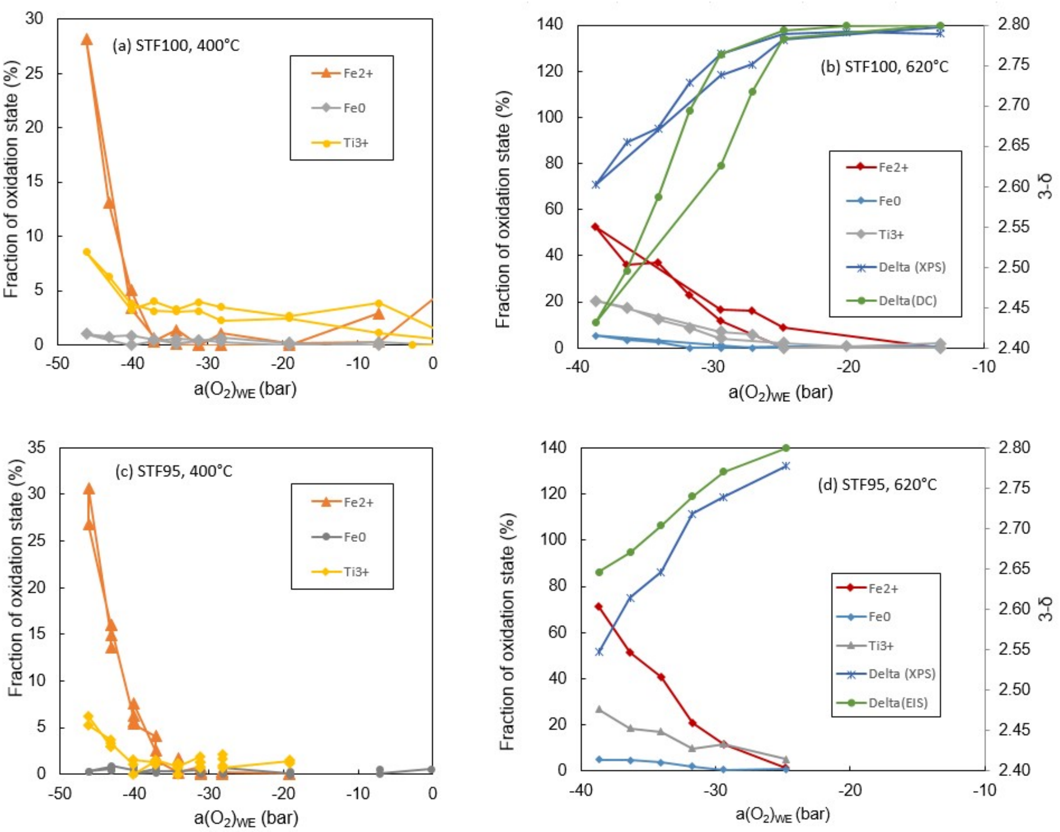

FIGURE 4.25: Quantification of different oxidation states of Fe and Ti. In contrast to the remaining work, oxygen non-stoichiometry is presented as $3-\delta$.

measured non-stoichiometry of STF100 and STF95. In summary, however, one can say that the surface reducibility according to XPS is in good quantitative agreement with the bulk-sensitive coulometry data. This observation is different to the well-studied case of pure and acceptor-doped ceria, for which higher surface reducibility has been found in many studies [39–41]. Hence, we can confirm the onset of Fe metal exsolution below 10^{-32} bar for both STF95 and STF100.

Moreover, the chemical composition of both samples was compared. For this, the peak areas of Fe 2p, Ti 2p and Sr 3d spectra were measured, and corrected for the analyser transmission function, inelastic mean free path, according to the TPP-2M equation [42] and empirically derived sensitivity factors according to Brundle and Christ [43]. Corrected signal intensities for Fe, Ti and Sr were then normalised to 100 %. No significant compositional changes were observed during reduction or oxidation, so the quantification presented in table 4.4 represents the mean value of all spectral data sets for better statistics. Although there is a slightly higher

Sr content for the STF100 sample, the difference is quite small. Interestingly, this finding apparently contradicts a previous investigation, in which strong A-site enrichment was found for stoichiometric STF and roughly cat % Sr for A-site deficient STF [44]. Potentially, slightly varying PLD conditions result in this discrepancy.

Table 4.4: Surface composition of STF100 and STF95

Sample	Fe (%)	Ti (%)	Sr (%)
STF100	13.6	29.3	57.1
STF95	14.1	30.2	55.8

Mechanistic interpretation of the irreversible processes

The characteristics of reductive phase transitions observed in powder and thin film coulometry differ substantially. This is primarily linked to two experimental differences: Firstly, the A-site sub-stoichiometric powders for coulometric titration were not phase pure, as evidenced by the phase transition at 10^{-24} bar. In contrast, none of the thin films exhibited such a steep step in the titration curves. Secondly, the direct electrochemical reduction allowed to apply much more reducing conditions, compared to the coulometric titration which could not get beyond 10^{-32} bar. Therefore, the thin film titration could also trigger irreversible processes in the STF phase, which happen below 10^{-32} bar. Also these processes are very subtle, indicating that the majority of the film remains intact perovskite-phase. In summary, three irreversible effects were observed.

1) The chemical capacitance peak at 10^{-33} bar decreases after the first reduction step (fig. 4.21). 2) The capacitance minimum in the stoichiometry plateau region is substantially higher after the first reduction (fig. 4.16b). 3) Only in the oxidation sweep, a capacitance peak around the oxygen activity of 10^{-24} bar could be observed (fig. 4.19b). These differences are stronger for the sub-stoichiometric compositions compared to the stoichiometric film, and we interpret them as follows: Fe ions in the STF lattice appear to be chemically quite stable, so strongly reducing contitions are required to trigger the exsolution of Fe metal, which is known to be irreversible. The exsolution of nanometer-sized Fe metal particles may explain all observed irreversible phenomena. The lower capacitance peak is in line with less Fe remaining in the perovskite phase. In other phases the reduction of Fe occurs much earlier. The capacitance minimum is largely defined by the concentration of electronic energy levels that lie within the band-gap of STF. Such energy levels may exist at cation vacancies, or grain and phase boundaries, that

emerge during the exsolution process. The capacitance peak (which is more pronounced in the coulometry data) in the oxidative direction is indicative for the oxidation of Fe metal to Fe oxide. The fact that this process is much less "sharp" than a real phase transition (which should be a delta function in the chemical capacitance) indicates that the formed Fe particles are real nanoparticles, with size-dependent oxidation enthalpy. Microscopic measurements with sufficient resolution will be required to resolve this in more detail.

4.3.4 Oxygen exchange activity of uncapped thin films

Thin film electrodes have proven to be an excellent model design to study the material-specific oxygen exchange kinetics of various SOFCs electrode materials, due to their simple geometry and controllable electronic and ionic current pathways, as shown by literature studies, e.g. on various SOFC cathode materials, [29] or acceptor doped ceria thin films as fuel electrodes [45], and also cation stoichiometric LSF and STF films in prior work from the Fleig research group [46–49] Uncapped samples were analysed with EIS under different gas atmospheres to study the effect of A-site sub-stoichiometry on the oxygen exchange activity of STF thin film electrodes. The impedance measurements under different atmospheres were carried out at 625°C with stoichiometric, as well as 3 % and 7 % sub-stoichiometric STF films simultaneously heated in a multiplexing impedance measurement setup. Per atmosphere step, 10 spectra were recorded of each sample. The atmosphere was cycled as follows: O_2, purging with N_2 for 300 min, H_2/H_2O, O_2, purging with N_2 for 300 min, H_2/H_2O. Electrochemical impedance spectra were fitted with ZView4®. The equivalent circuit used to fit the uncapped samples under reducing conditions is given in fig. 4.26.

The high frequency intercept was identified as a combination of the ionic transport resistance of the YSZ single crystal, as well as minor contributions of the resistance of the current collector and the resistance of the wiring. The remaining feature was fitted with two R/CPE elements and attributed to the working electrode, as additional measurements revealed the polarization resistance of the counter electrode to be negligibly small under reducing conditions. For measurements in oxidising conditions, however, the impedance spectra were often not trivial to interpret (an exemplary spectrum is presented in fig. 4.27). This is most likely due to a non-negligible counter electrode polarisation resistance, and the imperfect lithograpy of the current collectors (section 4.3.1), which may lead to overpotential losses due to ion conduction in the thin film - especially in-plane ion conduction above the current collector, as simulated in [50]. Due to these difficulties, we restrict our analysis of the results here only to the area specific resistance in reducing conditions. The area specific resistance of all measured sam-

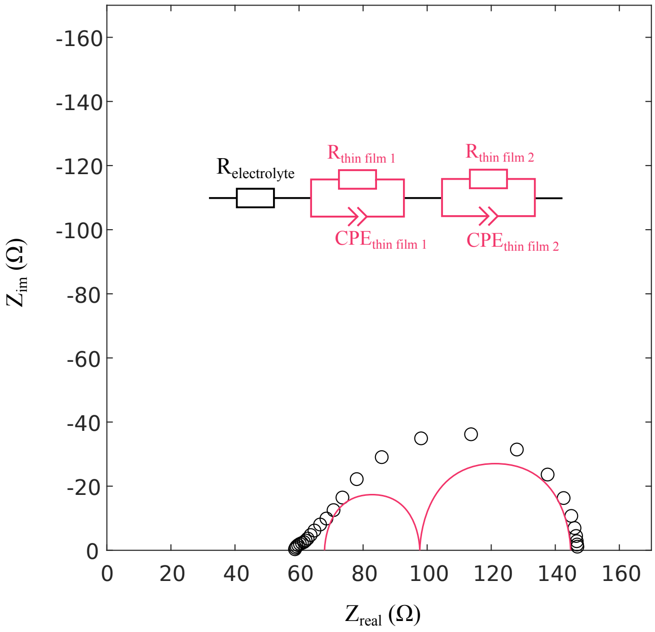

Figure 4.26: Exemplary impedance spectrum and corresponding equivalent circuit of the 7 % sub-stoichiometric uncapped thin film samples at 625 °C under reducing conditions. Coloured lines schematically show, which parts of the equivalent circuit represent which part of the impedance response.

ples is shown in fig. 4.28. As can be seen, the area specific resistance decreases with increasing sub-stoichiometry for the samples measured. However, the 7 % sub-stoichiometric sample does exhibit a clear increase in polarisation resistance upon the second reductive cycle.

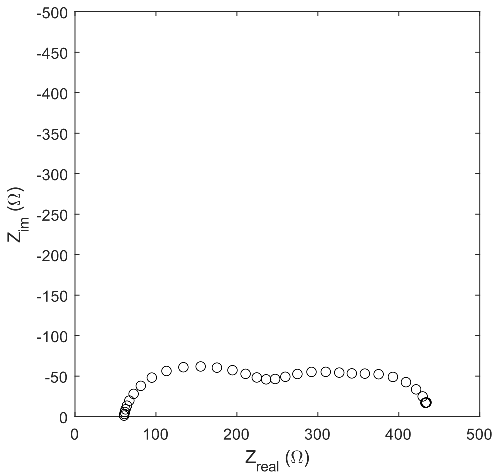

FIGURE 4.27: Exemplary impedance spectrum of the 7 % sub-stoichiometric uncapped samples at 625 °C under oxidising conditions with difficult to interpret features.

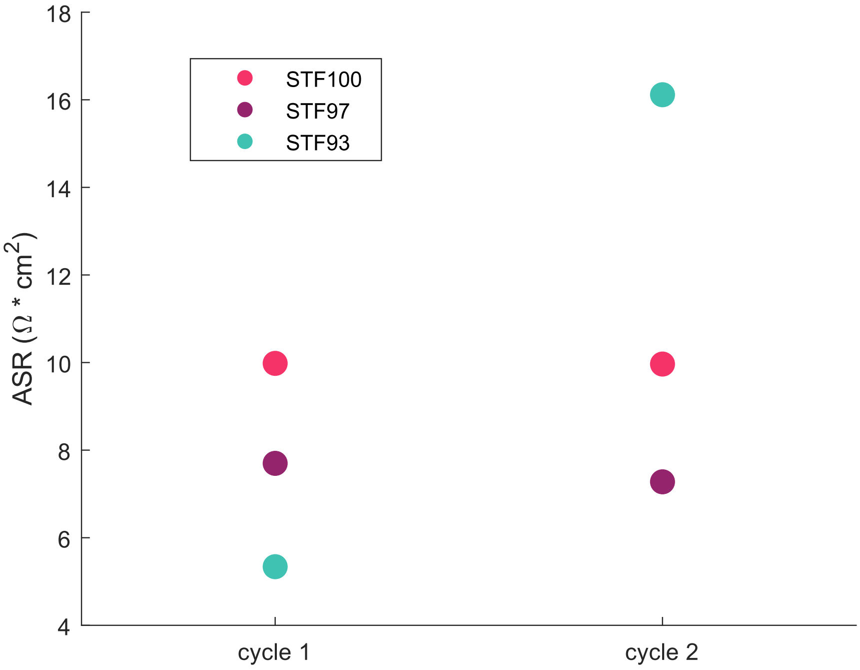

FIGURE 4.28: Area specific resistance of uncapped thin films in $\Omega \cdot cm^2$ at 625 °C.

5 Summary and Outlook

The effect of A-site sub-stoichiometry on the defect chemistry of perovskites was investigated. To that end, LSF and STF powder and STF thin film samples were used as model systems to study the pO_2 dependency of the oxygen non-stoichiometry. Powder samples were analysed using a new miniature coulometry cell that enables measurements of changes in oxygen stoichiometry over a wide range of pO_2. Noteworthy, the pO_2 accessible with this method lies below what is achievable with H_2 gas with H_2O traces. Different synthesis methods were compared, of which all showed degrees of a $SrFe_{12}O_{19}$ secondary phase at higher A-site deficiency in XRD measurements. Even for samples that appeared phase pure in the XRD, however, coulometry revealed the presence of a secondary phase. These secondary phases formed during the synthesis could be quantified with the presented methods. Dense thin film samples were prepared *via* PLD and analysed with EIS and coulometry. Measurements revealed a wide stability window for STF thin films, with Fe^{2+} being stable down to a pO_2 of 10^{-32} bar. Below this pressure exsolution of Fe nanoparticle could be observed. At this pO_2 even a partial reduction of Ti^{4+} to Ti^{3+} was possible. These results were backed up by XPS measurements. A strong effect of A-site deficiency on the exsolution behaviour of the studied materials could not be observed in these first measurements. Here, further studies are necessary to gain a more profound insight on the effect of A-site deficiency. For a precise interpretation of the measured changes in oxygen stoichiometry, it is important to know whether A-site deficiency is compensated by the formation of A-site vacancies or anti-site defects under the given conditions. This, however, could not be concluded from the presented data and additional measurements are needed to resolve this issue. EIS of STF thin films showed lower surface exchange resistances of A-site deficient materials under reducing conditions. However, fast degradation was observed for the sample with the highest A-site deficiency.

Danksagung

Wie den meisten Lesenden wohl bewusst ist, entsteht keine wissenschaftliche Arbeit in einem Vakuum (die gezeigten XPS Messungen vielleicht ausgenommen). Ich möchte daher diese Gelegenheit nutzen, um mich bei jenen Leuten zu bedanken, die maßgeblich (direkt und indirekt) am Entstehungsprozess dieser Arbeit beteiligt waren. Zunächst gilt mein Dank dem österreichischen Bildungssystem, welches mir (trotz mehrfacher Sabotageversuche durch verschiedene rechte Regierungsparteien) große Teile meines Studiums finanziert hat. Man könnte meinen, dass diese indirekte Erwähnung von knapp neun Millionen Personen für eine Danksagung bereits ausreichen sollte, dennoch möchte ich hier einige weitere wichtige Menschen besonders herausstreichen. Dank für die finanzielle Unterstützung bei meinem Studium gilt auch meiner Mutter, vielmehr aber noch für die große Freude, mit der sie mir bereits in jungen Jahren die Begeisterung für wissenschaftliche Denkweisen näher gebracht hat und ihre Hilfe dabei, mich in einer Gesellschaft zurecht zu finden, die sich so oft einem rationalen Verständnis entzieht. Ein weiterer großer Dank gilt meinem Freundeskreis, welcher mich während meines Studiums auf die vielfältigsten Arten unterstützt und, wann immer das notwendig war, abgelenkt hat. Besonderer Dank gilt auch der gesamten Arbeitsgruppe, in der ich mich hier wiedergefunden habe und von welcher ich herzlich aufgenommen wurde. Mein Dank gilt ihnen allen, auch wenn ich hier nur manche von ihnen exemplarisch anführe. Zuerst sei hier Jürgen angeführt, dafür, dass er mir die Arbeit in seiner Gruppe ermöglicht hat. An prominenter Stelle ist hier natürlich auch Andi zu nennen, der als mein Betreuer nicht nur eine nie enden wollende Geduld an den Tag gelegt hat und meine etwas unkonventionellen Eskapaden mit einem Lachen willkommen geheißen hat (auch wenn das bedeutete eine Messung zu unterbrechen um ein Brot aus dem Backrohr zu holen), sondern mich auch mit einer solchen Freude in die Arbeit hier eingeführt hat, dass meine Begeisterung für dieses Forschungsfeld mit jedem Tag gewachsen ist. Die faszienerenden wissenschaftlichen Erklärung und Einblicke, die mir in Gesprächen mit ihm geboten wurden, werden nur übertroffen von dem Blick für absurde, simple Lösungen für komplexe Probleme, den er versucht hat an mich weiter zu geben. Kirsten für die vielfältigen Inspirationen, die SEM Messungen (inklusiver der tollen Probenbenennung) und dafür, dass sie mich in den schwierigeren Stunden meines Masterstudiums mit allen Mitteln versucht hat wach zu halten. Auch Joseph gilt mein Dank für die SEM Messungen (und die Begeisterung, die er dabei weitergeben konnte) sowie die geteilte Faszination für gutes Essen. Melli, die immer zum gemeinsam sudern zu haben war. Babs, ohne die diese Masterarbeit wahrscheinlich noch immer ein einziger unformatierte Haufen wäre. Christian, der immer offen für angeregte fachliche Diskussionen war (und mir die vergangenen zwei Monate das Einkaufen gehen erspart hat). Max und Udo für ihre ausgiebige kulinarische Unterstützung. Eva für ihre administrative Hilfe, ohne sie würde ich hier wohl noch immer vor lauter verschlossenen Türen stehen. Mina, die unser Büro mit Unmengen an positiver Energie und den gelegentlichen Süßigkeiten versorgt hat. Christin, die für jedes noch so unüberwindbar scheinende Problem einen guten Lösungsansatz gefunden hat, durchdachte Anregungen zur Struktur dieser Arbeit geliefert hat, mir zahlreiche Stunden im Kampf mit Informationstechnologie zur Seite gestanden ist und noch so vieles mehr. Außerdem hat sie sich selbst zu den ausgefallensten Kochprojekten überreden lassen. Claudia für die Hartnäckigkeit, die sie bei den ICP-MS Messungen an den Tag gelegt hat (noch haben wir nicht aufgegeben) und ihre nicht enden wollende Hilfsbereitschaft.

Last but not least möchte ich mich bei Samuel bedanken. Ohne dich wäre das Studium nur halb so lustig (und auch nur halb so schnell) gewesen!

Danke!

Acronyms

BSE Backscattered Electron. 19

CPE Constant Phase Element. 32, 33, 66

EIS Electrochemical Impedance Spectroscopy. 2, 22, 24, 34, 50–52, 56, 60, 63, 66, 69

FWHM Full Width Half Maximum. 62

GDC Gd:CeO_2. 15, 16, 25, 27, 47

ICP-MS Inductively Coupled Plasma Mass Spectrometry. 2, 19, 40, 71

LSF $La_{1-x}Sr_xFeO_{3-\delta}$. 2, 7, 13, 29, 35, 36, 39, 40, 42, 43, 66, 69

MIECs Mixed Ion Electron Conductors. 3

PCO Pr:CeO_2. 20

PLD Pulsed Laser Deposition. 2, 15, 17, 41, 65, 69

SE Secondary Electron. 19

SEM Scanning Electron Microscope. 19, 47–49, 70, 71

SFO $SrFeO_{2.5}$. 8

SOECs Solid Oxide Electrolysis Cells. 1, 3, 6

SOFCs Solid Oxide Fuel Cells. 1, 3, 6, 66

STF $SrTi_{1-x}Fe_xO_{3-\delta}$. 2, 8, 13, 15, 17, 18, 25, 26, 29, 40–42, 46–48, 50, 52, 55, 56, 65, 66, 69

STO $SrTiO_3$. 8

XPS X-Ray Photoelectron Spectroscopy. 2, 25–27, 34, 46, 47, 55, 60, 61, 63, 64, 69, 70

XRD X-Ray Diffraction. 20, 35, 36, 39–41, 46, 69

YSZ Yttria Stabilized Zirconia. 1, 15, 16, 20, 26, 31, 32, 47, 66

Bibliography

[1] J. W. Fergus. "Materials challenges for solid-oxide fuel cells". In: *JOM* 59.12 (Dec. 2007), pp. 56–62. DOI: `10.1007/s11837-007-0153-x`.

[2] B. Koo, K. Kim, J. K. Kim, H. Kwon, J. W. Han, and W. Jung. "Sr Segregation in Perovskite Oxides: Why It Happens and How It Exists". In: *Joule* 2.8 (Aug. 2018), pp. 1476–1499. DOI: `10.1016/j.joule.2018.07.016`.

[3] Z. Cai, M. Kubicek, J. Fleig, and B. Yildiz. "Chemical Heterogeneities on $La_{0.6}Sr_{0.4}CoO_{3-\delta}$ Thin Films—Correlations to Cathode Surface Activity and Stability". In: *Chemistry of Materials* 24.6 (Mar. 2012), pp. 1116–1127. DOI: `10.1021/cm203501u`.

[4] A.-K. Huber, M. Falk, M. Rohnke, B. Luerssen, M. Amati, L. Gregoratti, D. Hesse, and J. Janek. "In situ study of activation and de-activation of LSM fuel cell cathodes – Electrochemistry and surface analysis of thin-film electrodes". In: *Journal of Catalysis* 294 (Oct. 2012), pp. 79–88. DOI: `10.1016/j.jcat.2012.07.010`.

[5] M. Siebenhofer, A. Nenning, G. E. Wilson, J. A. Kilner, C. Rameshan, M. Kubicek, J. Fleig, and P. Blaha. "Electronic and ionic effects of sulphur and other acidic adsorbates on the surface of an SOFC cathode material". In: *Journal of Materials Chemistry A* 11.13 (2023), pp. 7213–7226. DOI: `10.1039/d3ta00978e`.

[6] H. Summerer, A. Nenning, C. Rameshan, and A. K. Opitz. "Exsolved catalyst particles as a plaything of atmosphere and electrochemistry". In: *EES Catalysis* 1.3 (2023), pp. 274–289. DOI: `10.1039/d2ey00036a`.

[7] G. Tsekouras, D. Neagu, and J. T. S. Irvine. "Step-change in high temperature steam electrolysis performance of perovskite oxide cathodes with exsolution of B-site dopants". In: *Energy Environ. Sci.* 6.1 (2013), pp. 256–266. DOI: `10.1039/c2ee22547f`.

[8] J. Li, Y. Yu, Y.-M. Yin, N. Zhou, and Z.-F. Ma. "A novel high performance composite anode with in situ growth of Fe-Ni alloy nanoparticles for intermediate solid oxide fuel cells". In: *Electrochimica Acta* 235 (May 2017), pp. 317–322. DOI: `10.1016/j.electacta.2017.03.103`.

[9] L. Lindenthal, J. Popovic, R. Rameshan, J. Huber, F. Schrenk, T. Ruh, A. Nenning, S. Löffler, A. Opitz, and C. Rameshan. "Novel perovskite catalysts for CO_2 utilization - Exsolution enhanced reverse water-gas shift activity". In: *Applied Catalysis B: Environmental* 292 (Sept. 2021), p. 120183. DOI: `10.1016/j.apcatb.2021.120183`.

[10] Y. Gao, D. Chen, M. Saccoccio, Z. Lu, and F. Ciucci. "From material design to mechanism study: Nanoscale Ni exsolution on a highly active A-site deficient anode material for solid oxide fuel cells". In: *Nano Energy* 27 (Sept. 2016), pp. 499–508. DOI: `10.1016/j.nanoen.2016.07.013`.

[11] D. Neagu, G. Tsekouras, D. N. Miller, H. Ménard, and J. T. S. Irvine. "In situ growth of nanoparticles through control of non-stoichiometry". In: *Nature Chemistry* 5.11 (Oct. 2013), pp. 916–923. DOI: `10.1038/nchem.1773`.

[12] Y. Sun, J. Li, Y. Zeng, B. S. Amirkhiz, M. Wang, Y. Behnamian, and J. Luo. "A-site deficient perovskite: the parent for in situ exsolution of highly active, regenerable nano-particles as SOFC anodes". In: *Journal of Materials Chemistry A* 3.20 (2015), pp. 11048–11056. DOI: `10.1039/c5ta01733e`.

[13] D. Neagu, T.-S. Oh, D. N. Miller, H. Ménard, S. M. Bukhari, S. R. Gamble, R. J. Gorte, J. M. Vohs, and J. T. Irvine. "Nano-socketed nickel particles with enhanced coking resistance grown *in situ* by redox exsolution". In: *Nature Communications* 6.1 (Sept. 2015). DOI: `10.1038/ncomms9120`.

[14] J.-H. Zhang, F.-Z. Han, C.-X. Li, and S.-L. Zhang. "A-site deficient $Sr_{0.9}Ti_{0.3}Fe_{0.7}O_{3-\delta}$ perovskite: A high stable cobalt-free oxygen electrode material for solid oxide electrochemical cells with excellent electrocatalytic activity and CO_2 tolerance". In: *Journal of the European Ceramic Society* 42.13 (Oct. 2022), pp. 5801–5812. DOI: `10.1016/j.jeurceramsoc.2022.06.047`.

[15] H. Yang, M. B. Hanif, S.-L. Zhang, C.-J. Li, and C.-X. Li. "Sintering behavior and electrochemical performance of A-site deficient $Sr_xTi_{0.3}Fe_{0.7}O_{3-\delta}$ oxygen electrodes for solid oxide electrochemical cells". In: *Ceramics International* 47.17 (Sept. 2021), pp. 25051–25058. DOI: `10.1016/j.ceramint.2021.05.235`.

[16] K. Chu, F. Liu, J. Zhu, H. Fu, H. Zhu, Y. Zhu, Y. Zhang, F. Lai, and T. Liu. "A General Strategy to Boost Electrocatalytic Nitrogen Reduction on Perovskite Oxides via the Oxygen Vacancies Derived from A-Site Deficiency". In: *Advanced Energy Materials* 11.11 (Jan. 2021), p. 2003799. DOI: `10.1002/aenm.202003799`.

[17] Y. Gao, J. Wang, Y.-Q. Lyu, K. Lam, and F. Ciucci. “*In situ* growth of Pt_3Ni nanoparticles on an A-site deficient perovskite with enhanced activity for the oxygen reduction reaction”. In: *Journal of Materials Chemistry A* 5.14 (2017), pp. 6399–6404. DOI: `10.1039/c7ta00349h`.

[18] F. Kröger and H. Vink. “Relations between the Concentrations of Imperfections in Crystalline Solids”. In: *Solid State Physics*. Elsevier, 1956, pp. 307–435. DOI: `10.1016/s0081-1947(08)60135-6`.

[19] A. Braun, D. Bayraktar, S. Erat, A. S. Harvey, D. Beckel, J. A. Purton, P. Holtappels, L. J. Gauckler, and T. Graule. “Pre-edges in oxygen (1s) x-ray absorption spectra: A spectral indicator for electron hole depletion and transport blocking in iron perovskites”. In: *Applied Physics Letters* 94.20 (May 2009). DOI: `10.1063/1.3122926`.

[20] Y. Li, W. Zhang, Y. Zheng, J. Chen, B. Yu, Y. Chen, and M. Liu. “Controlling cation segregation in perovskite-based electrodes for high electro-catalytic activity and durability”. In: *Chemical Society Reviews* 46.20 (2017), pp. 6345–6378. DOI: `10.1039/c7cs00120g`.

[21] J.-h. Myung, D. Neagu, D. N. Miller, and J. T. S. Irvine. “Switching on electrocatalytic activity in solid oxide cells”. In: *Nature* 537.7621 (Aug. 2016), pp. 528–531. DOI: `10.1038/nature19090`.

[22] Z. Du, H. Zhao, S. Yi, Q. Xia, Y. Gong, Y. Zhang, X. Cheng, Y. Li, L. Gu, and K. Świerczek. “High-Performance Anode Material $Sr_2FeMo_{0.65}Ni_{0.35}O_{6-\delta}$ with *In Situ* Exsolved Nanoparticle Catalyst”. In: *ACS Nano* 10.9 (Aug. 2016), pp. 8660–8669. DOI: `10.1021/acsnano.6b03979`.

[23] M. Kuhn, S. Hashimoto, K. Sato, K. Yashiro, and J. Mizusaki. “Oxygen nonstoichiometry, thermo-chemical stability and lattice expansion of $La_{0.6}Sr_{0.4}FeO_{3-\delta}$”. In: *Solid State Ionics* 195.1 (July 2011), pp. 7–15. DOI: `10.1016/j.ssi.2011.05.013`.

[24] L. Brixner. “Preparation and properties of the $SrTi_{1-x}Fe_xO_{3-x2}/O_{x2}$ system”. In: *Materials Research Bulletin* 3.4 (Apr. 1968), pp. 299–308. DOI: `10.1016/0025-5408(68)90001-9`.

[25] A. Rothschild, W. Menesklou, H. L. Tuller, and E. Ivers-Tiffée. “Electronic Structure, Defect Chemistry, and Transport Properties of $SrTi_{1-x}Fe_xO_{3-y}$ Solid Solutions”. In: *Chemistry of Materials* 18.16 (July 2006), pp. 3651–3659. DOI: `10.1021/cm052803x`.

[26] A. Ferreira. “Oxygen stoichiometry of $Sr_{0.97}(Ti,Fe)O_{3-\delta}$ materials”. In: *Solid State Ionics* 135.1-4 (Nov. 2000), pp. 761–764. DOI: `10.1016/s0167-2738(00)00375-1`.

[27] M. Kuhn, J. J. Kim, S. R. Bishop, and H. L. Tuller. “Oxygen Nonstoichiometry and Defect Chemistry of Perovskite-Structured $Ba_xSr_{1-x}Ti_{1-y}Fe_yO_{3-y/2+\delta}$ Solid Solutions”. In: *Chemistry of Materials* 25.15 (July 2013), pp. 2970–2975. DOI: `10.1021/cm400546z`.

[28] M. Morgenbesser, A. Viernstein, A. Schmid, C. Herzig, M. Kubicek, S. Taibl, G. Bimashofer, J. Stahn, C. A. F. Vaz, M. Döbeli, F. Biautti, J. de Dios Sirvent, M. O. Liedke, M. Butterling, M. Kamiński, M. Tolkiehn, V. Vonk, A. Stierle, A. Wagner, A. Tarancon, A. Limbeck, and J. Fleig. “Unravelling the Origin of Ultra-Low Conductivity in $SrTiO_3$ Thin Films: Sr Vacancies and Ti on A-Sites Cause Fermi Level Pinning”. In: *Advanced Functional Materials* 32.38 (July 2022), p. 2202226. DOI: `10.1002/adfm.202202226`.

[29] F. S. Baumann, J. Fleig, G. Cristiani, B. Stuhlhofer, H.-U. Habermeier, and J. Maier. “Quantitative Comparison of Mixed Conducting SOFC Cathode Materials by Means of Thin Film Model Electrodes”. In: *Journal of The Electrochemical Society* 154.9 (2007), B931. DOI: `10.1149/1.2752974`.

[30] C. Ahamer, A. K. Opitz, G. M. Rupp, and J. Fleig. “Revisiting the Temperature Dependent Ionic Conductivity of Yttria Stabilized Zirconia (YSZ)”. In: *Journal of The Electrochemical Society* 164.7 (2017), F790–F803. DOI: `10.1149/2.0641707jes`.

[31] R. D. Holmes, H. S. O’Neill, and R. J. Arculus. “Standard Gibbs free energy of formation for Cu_2O, NiO, CoO, and FexO: High resolution electrochemical measurements using zirconia solid electrolytes from 900–1400 K”. In: *Geochimica et Cosmochimica Acta* 50.11 (Nov. 1986), pp. 2439–2452. DOI: `10.1016/0016-7037(86)90027-x`.

[32] A. Nenning and J. Fleig. “Electrochemical XPS investigation of metal exsolution on SOFC electrodes: Controlling the electrode oxygen partial pressure in ultra-high-vacuum”. In: *Surface Science* 680 (Feb. 2019), pp. 43–51. DOI: `10.1016/j.susc.2018.10.006`.

[33] J.-H. Park and R. N. Blumenthal. “Electronic Transport in 8 Mole Percent $Y_2O_3-ZrO_2$”. In: *Journal of The Electrochemical Society* 136.10 (Oct. 1989), pp. 2867–2876. DOI: `10.1149/1.2096302`.

[34] T. Striker, J. Ruud, Y. Gao, W. Heward, and C. Steinbruchel. “A-site deficiency, phase purity and crystal structure in lanthanum strontium ferrite powders”. In: *Solid State Ionics* 178.21-22 (July 2007), pp. 1326–1336. DOI: `10.1016/j.ssi.2007.06.011`.

[35] A. K. Opitz, A. Nenning, V. Vonk, S. Volkov, F. Bertram, H. Summerer, S. Schwarz, A. Steiger-Thirsfeld, J. Bernardi, A. Stierle, and J. Fleig. “Understanding electrochemical switchability of perovskite-type exsolution catalysts”. In: *Nature Communications* 11.1 (Sept. 2020). DOI: `10.1038/s41467-020-18563-w`.

[36] A. Nenning, A. K. Opitz, C. Rameshan, R. Rameshan, R. Blume, M. Hävecker, A. Knop-Gericke, G. Rupprechter, B. Klötzer, and J. Fleig. “Ambient Pressure XPS Study of Mixed Conducting Perovskite-Type SOFC Cathode and Anode Materials under Well-Defined Electrochemical Polarization”. In: *The Journal of Physical Chemistry C* 120.3 (Jan. 2016), pp. 1461–1471. DOI: `10.1021/acs.jpcc.5b08596`.

[37] M. Descostes, F. Mercier, N. Thromat, C. Beaucaire, and M. Gautier-Soyer. “Use of XPS in the determination of chemical environment and oxidation state of iron and sulfur samples: constitution of a data basis in binding energies for Fe and S reference compounds and applications to the evidence of surface species of an oxidized pyrite in a carbonate medium”. In: *Applied Surface Science* 165.4 (Oct. 2000), pp. 288–302. DOI: `10.1016/s0169-4332(00)00443-8`.

[38] M. C. Biesinger, B. P. Payne, A. P. Grosvenor, L. W. Lau, A. R. Gerson, and R. S. Smart. “Resolving surface chemical states in XPS analysis of first row transition metals, oxides and hydroxides: Cr, Mn, Fe, Co and Ni”. In: *Applied Surface Science* 257.7 (Jan. 2011), pp. 2717–2730. DOI: `10.1016/j.apsusc.2010.10.051`.

[39] W. C. Chueh, A. H. McDaniel, M. E. Grass, Y. Hao, N. Jabeen, Z. Liu, S. M. Haile, K. F. McCarty, H. Bluhm, and F. E. Gabaly. “Highly Enhanced Concentration and Stability of Reactive Ce^{3+} on Doped CeO_2 Surface Revealed In Operando”. In: *Chemistry of Materials* 24.10 (May 2012), pp. 1876–1882. DOI: `10.1021/cm300574v`.

[40] C. Zhang, M. E. Grass, Y. Yu, K. J. Gaskell, S. C. DeCaluwe, R. Chang, G. S. Jackson, Z. Hussain, H. Bluhm, B. W. Eichhorn, and Z. Liu. “Multielement Activity Mapping and Potential Mapping in Solid Oxide Electrochemical Cells through the use of *operando* XPS”. In: *ACS Catalysis* 2.11 (Sept. 2012), pp. 2297–2304. DOI: `10.1021/cs3004243`.

[41] S. Bishop, K. Duncan, and E. Wachsman. “Surface and bulk oxygen non-stoichiometry and bulk chemical expansion in gadolinium-doped cerium oxide”. In: *Acta Materialia* 57.12 (July 2009), pp. 3596–3605. DOI: `10.1016/j.actamat.2009.04.017`.

[42] S. Tanuma, C. J. Powell, and D. R. Penn. “Calculation of electron inelastic mean free paths (IMFPs) VII. Reliability of the TPP-2M IMFP predictive equation”. In: *Surface and Interface Analysis* 35.3 (2003), pp. 268–275. DOI: `10.1002/sia.1526`.

[43] C. R. Brundle and B. V. Crist. “X-ray photoelectron spectroscopy: A perspective on quantitation accuracy for composition analysis of homogeneous materials”. In: *Journal of Vacuum Science &amp Technology A: Vacuum, Surfaces, and Films* 38.4 (June 2020). DOI: `10.1116/1.5143897`.

[44] W. Jung and H. L. Tuller. “Investigation of surface Sr segregation in model thin film solid oxidefuel cell perovskite electrodes”. In: *Energy Environ. Sci.* 5.1 (2012), pp. 5370–5378. DOI: `10.1039/c1ee02762j`.

[45] Z. A. Feng, F. E. Gabaly, X. Ye, Z.-X. Shen, and W. C. Chueh. “Fast vacancy-mediated oxygen ion incorporation across the ceria–gas electrochemical interface”. In: *Nature Communications* 5.1 (July 2014). DOI: `10.1038/ncomms5374`.

[46] S. Kogler, A. Nenning, G. M. Rupp, A. K. Opitz, and J. Fleig. “Comparison of Electrochemical Properties of $La_{0.6}Sr_{0.4}FeO_{3-\delta}$ Thin Film Electrodes: Oxidizing vs. Reducing Conditions”. In: *Journal of The Electrochemical Society* 162.3 (2015), F317–F326. DOI: `10.1149/2.0731503jes`.

[47] A. Nenning, L. Volgger, E. Miller, L. V. Mogni, S. Barnett, and J. Fleig. “The Electrochemical Properties of $Sr(Ti,Fe)O_{3-\delta}$ for Anodes in Solid Oxide Fuel Cells”. In: *Journal of The Electrochemical Society* 164.4 (2017), F364–F371. DOI: `10.1149/2.1271704jes`.

[48] A. Schmid, G. M. Rupp, and J. Fleig. “Voltage and partial pressure dependent defect chemistry in $(La,Sr)FeO_{3-\delta}$ thin films investigated by chemical capacitance measurements”. In: *Physical Chemistry Chemical Physics* 20.17 (2018), pp. 12016–12026. DOI: `10.1039/c7cp07845e`.

[49] A. Schmid, A. Nenning, A. Opitz, M. Kubicek, and J. Fleig. “High Oxygen Exchange Activity of Pristine $La_{0.6}Sr_{0.4}FeO_{3-\delta}$ Films and Its Degradation”. In: *Journal of The Electrochemical Society* 167.12 (Jan. 2020), p. 124509. DOI: `10.1149/1945-7111/abac2b`.

[50] A. Nenning, A. K. Opitz, T. M. Huber, and J. Fleig. “A novel approach for analyzing electrochemical properties of mixed conducting solid oxide fuel cell anode materials by impedance spectroscopy”. In: *Phys. Chem. Chem. Phys.* 16.40 (2014), pp. 22321–22336. DOI: `10.1039/c4cp02467b`.